The GFDL Variable-Resolution Global Chemistry-Climate Model for Research at the Nexus of US Climate and Air Quality Extremes

Meiyun Lin[1][*], Larry W. Horowitz[1], Ming Zhao[1], Lucas Harris[1], Paul Ginoux[1], John Dunne[1], Sergey Malyshev[1], Elena Shevliakova[1], Hamza Ahsan[2], Steve Garner[1], Fabien Paulot[1], Arman Pouyaei[3], Steven J. Smith[2], Yuanyu Xie[4], Niki Zadeh[1], Linjiong Zhou[3]

[1] NOAA Geophysical Fluid Dynamics Laboratory, Princeton, NJ, USA
[2] Joint Global Change Research Institute, Pacific Northwest National Laboratory, College Park, MD, USA
[3] Cooperative Institute for Modeling the Earth System, Princeton University, Princeton, NJ, USA
[4] Princeton School of Public and International Affairs, Princeton University, Princeton, NJ, USA

*Corresponding author: Meiyun Lin (Meiyun.Lin@noaa.gov)

This document includes Supplementary Text S1 to S7, Tables S1 and S2, and Figures S1 to S25 not included in the main article.

Text S1 Computational burden

The computational cost of AM4VR is ~90k compute hours per simulated year (CHSY; Balaji et al., 2017) using 3072 Cray XC40-LC Haswell cores on the "c3" partition of NOAA's Gaea supercomputer. The model scales well to additional processors, using ~119k CHSY on 6144 cores (on "c3"), or ~115k CHSY on 12,288 Cray XC40-LC Broadwell cores ("c4" partition). For comparison, the computational cost of the C96-resolution AM4 is ~4.7k CHSY on 1728 cores ("c3"), while the cost of the C384-resolution model is ~184k CHSY on 3456 cores ("c3").

Text S2 Aerosol optical properties

The optical properties of aerosol, extinction efficiency, single scattering albedo and asymmetry parameter, are calculated at 40 wavelengths from 174 nm to 40 micrometers using a Mie code as particles are assumed spherical with the additional following properties.

- DUST: The refractive index from 290 to 3710 nm is based on Balkanski et al. (2007) assuming 2.7% hematite content; and in the infrared from Volz (1973). There is no hygroscopic growth of dust. The size distribution within each 5 bins (radius ranges: 0.1-1, 1-1.8, 1.803, 3-6, 6-10 micrometers) are dM/dlnR=0, with the corresponding density of 2.5, 2.6, 2.6, 2.6, and 2.6 g/cm^3, respectively.
- SEA SALT: The refractive index for all wavelengths is based on Tang et al. (1997). Hygroscopic growth is based on Tang et al. (1997) assuming pure sodium chloride. The size distribution within each 5 bins (radius ranges: 0.01-0.5, 0.5-1, 1-2.5, 2.5-5, 5-10 micrometers) are dM/dlnR=0, with a dry density of 2.16 g/cm^3 for all bins.
- SULFATE: The refractive index at all wavelengths is based on Haywood and Ramaswamy (1997). The size distribution is assumed log-normal with a geometric mean radius of 0.05

micrometer and a standard deviation of 2. The hygroscopic growth is based on Tang and Munkelwitz (1994) assuming pure ammonium sulfate. The dry density is 1.769 g/cm^3.

- NITRATE: NH_4NO_3 optical properties are obtained from Mie calculations using hygroscopic growth from Tang [1996] and refractive indices from Gosse et al. [1997]. The impact of nitrate aerosols on clouds are treated as that for sulfate.
- BLACK CARBON: The refractive index at all wavelengths is based on Haywood and Ramaswamy (1997). The size distribution is assumed log-normal with a geometric mean radius of 0.0118 micrometer and a standard deviation of 2. The dry density is 1 g/cm^3. There is no hygroscopic growth of hydrophobic black carbon. But hydrophilic black-carbon is assumed internally mixed with sulfate and the refractive index of the mixture is calculated by volume-weighted average.
- ORGANIC CARBON: The refractive index at all wavelengths is based on Hess et al. (1998). The size distribution is assumed log-normal with a geometric mean radius of 0.085 micrometer and a standard deviation of 1.492.The dry density is 1.8 g/cm^3. There is no hygroscopic growth of hydrophobic organic carbon. But hydrophilic organics (primary and secondary) are assumed to be a mixture of acids and insoluble organics growing hygroscopically as in Ming and Russell (2004).

Text S3 Emissions of other BVOCs from vegetation

Figure 2e-f compares annual mean emission fluxes for other BVOCs prescribed for AM4.1 and AM4VR. Emissions of other BVOCs in AM4.1 are based on the Precursors of Ozone and their Effects in the Troposphere (POET) inventory (1°x1^o) for the year 2000. For AM4VR, we apply inter-annually varying emissions for 2000-2020, based on the data set of Sindelarova et al. [2022], developed in support of Copernicus Atmosphere Monitoring Service (CAMS-GLOB-BIO v3.1, 0.25^{o}x0.25^o). The 2000-2020 monthly climatology is applied for years before 2000. Annual total emissions of other BVOCs over CONUS are 10.6 TgC in AM4.1 and 8.3 ± 0.4 TgC/yr in AM4VR. The global totals are of similar magnitude (113.0-114.0 TgC/yr) between AM4.1 and AM4VR, but with notable differences in spatial distributions (**Fig.S8**). The new dataset for AM4VR provides more realistic distributions, with BVOC emissions more concentrated in the tropics and lower in the northern hemisphere boreal regions (**Fig.2e-f and Fig.S8**). AM4VR applies the same climatological emissions of NO$_x$, CO, and ammonia (NH$_3$) from nature as considered by Horowitz et al. [2020] for AM4.1.

Text S4: Updates in NMVOC emissions and SOA

AM4.1 does not account for direct emissions of acetaldehyde (CH_3CHO) and methyl ethyl ketone (MEK, $C_2H_5C(O)CH_3$); both are important PAN precursors known to have large emissions from biomass burning [Jaffe et al., 2020]. We update speciation of biomass burning, anthropogenic, and biogenic emissions of NMVOCs in AM4VR: (1) add emissions for CH_3CHO and MEK; (2) partition total ketone emissions from anthropogenic sources into acetone (C_3H_6O, 88%) and MEK (12%) according to the ratio from NEI2017; (3) correct a unit conversion error in AM4.1 emission processing script for C_4H_{10} and C_3H_6. This error resulted in biomass burning emissions in AM4.1 being four times too high for C_4H_{10} and ~50% too high for C_3H_6 (**Fig.S9**). C_4H_{10} is treated as a precursor to anthropogenic and biomass burning SOA in the models. AM4VR assumes a 20% per-carbon SOA yield (increasing from 10% in AM4.1) from oxidation of the simulated C_4H_{10} hydrocarbon tracer by hydroxyl radical. The higher yield is more consistent with a recent review of laboratory studies [Wang et al., 2020; Srivastava et al., 2022].

Text S5: Bias correction of TROPOMI HCHO data

Launched on board of the European Copernicus Sentinel-5 Precursor (S5P) satellite in October 2017, the TROPOspheric Monitoring Instrument (TROPOMI, Veefkind et al., 2012) improves the precision of the HCHO observations at short temporal scales and for low HCHO levels compared with the previous OMI retrieval, but OMI and TROPOMI data present equivalent biases for large HCHO levels [De Smedt et al., 2021]. Following the approach of Kaiser et al. [2018] based on validation of OMI with independent aircraft measurements, we apply a 37% bias correction to monthly TROPOMI data (0.05°x0.05°) provided by De Smedt et al. [2021] for 2018-2020. For each 0.05°x0.05° grid within the CONUS domain with HCHO columns larger than $1.2x10^{16}$ molecules.cm^2, a multiplicative factor of $1/(1-0.37) = 1.59$ is applied to TROPOMI data. The bias-corrected TROPOMI HCHO observations are then averaged over June-August 2018-2020 and regridded to 13 km resolution for comparison with AM4VR sampled at TROPOMI overpass time (1:30PM).

Text S6: Changes in diagnostic outputs for atmospheric tracer concentrations

The diagnostic output for atmospheric tracer concentrations, including that for hourly surface ozone, was modified in the model results shown in the present study. In AM4.1, these diagnostics were output during the timestep loop, following the dry deposition sub-step, but before emissions and chemistry. As such, the surface ozone concentrations output from the model were artificially reduced [Horowitz et al., 2020]. In AM4VR, these concentrations are output prior to adding the deposition (which is now computed in the land component), emissions, and chemistry tendencies, avoiding the numerical issues reducing surface ozone concentrations in AM4.1. To ensure an apple-to-apple comparison, we rerun AM4.1 with the hourly surface ozone output configured as in AM4VR. Reflecting these changes in diagnostic outputs, surface ozone concentrations in AM4.1 shown in the present study are different from those reported previously in Horowitz et al. [2020].

Text S7: Correction of simulated near-surface ozone concentrations

Computation of ozone at the 2-m level is based on interpolation between the lowest model level and the surface:

tr_ref = tr_surf + (tr_atm - tr_surf) * del_q

Where tr_ref is the tracer field at the 2m reference height, tr_surf is the near-surface exchange flux, tr_atm is the exchange flux in the lowest atmospheric layer; and del_q is the reference height interpolation factor - the same as that used for computing humidity at the 2m level in the model. Computation of del_q considers surface roughness, wind speed, and atmospheric stability using Monin–Obukhov similarity theory, similar to the approach described in detail by ECMWF [2016]. Calculated summer MDA8 ozone at the 2m level from AM4VR are shown in Fig.25e-f and Fig.26a for comparison with AQS observations, as discussed in the main article. The difference in MDA8 ozone between the 2m level and the lowest model layer is reported in Fig.S25. The remainder of the figures in this article is based on ozone in the lowest model layer consistent between AM4VR and AM4.1.

Supplemental References:

Balaji, V, E Maisonnave, Niki Zadeh, B N Lawrence, Joachim Biercamp, U Fladrich, G Aloisio, Rusty Benson, A Caubel, Jeffrey W Durachta, M-A Foujols, G Lister, S Mocavero, Seth D Underwood, and Garrett Wright, January 2017: CPMIP: Measurements of Real Computational Performance of Earth System Models. Geoscientific Model Development, 10(1), DOI:10.5194/gmd-10-19-2017.

Balkanski, Y., Schulz, M., Claquin, T., and Guibert, S.: Reevaluation of Mineral aerosol radiative forcings suggests a better agreement with satellite and AERONET data, Atmos. Chem. Phys., 7, 81–95, https://doi.org/10.5194/acp-7-81-2007, 2007.

ECMWF (2016). IFS DOCUMENTATION – Cy43r1 Operational implementation 22 Nov 2016. PART IV: PHYSICAL PROCESSES. https://www.ecmwf.int/sites/default/files/elibrary/2016/17117-part-iv-physical-processes.pdf#subsection.3.10.3

Gosse, S. F., M. Wang, D. Labrie, and P. Chylek (1997), Imaginary part of the refractive index of sulfates and nitrates in the 07–26-μm spectral region, *Appl. Opt.*, 36, 3622–3634.

Haywood, J. M., and V. Ramaswamy, 1998: Global sensitivity studies of the direct radiative forcing due to anthropogenic sulfate and black carbon aerosols. J. Geophys. Res., 103, 6043–6058.

Hess, M., P. Koepke, and I. Schult, 1998: Optical properties of aerosols and clouds: The software package OPAC. *Bull. Amer. Meteor. Soc.*, **79**, 831–844.

Ming, Y., and L. M. Russell, 2004: Organic aerosol effects on fog droplet spectra. *J. Geophys. Res.*, **109**, D10206, doi:10.1029/2003JD004427.

Srivastava, D., Vu, T.V., Tong, S. et al. Formation of secondary organic aerosols from anthropogenic precursors in laboratory studies. npj Clim Atmos Sci 5, 22 (2022). https://doi.org/10.1038/s41612-022-00238-6

Tang, I. N. (1996), Chemical and size effects of hygroscopic aerosols on light scattering coefficients, *J. Geophys. Res.*, 101, 19,245–19,250.

Tang, I. N., A. C. Tridico, and K. H. Fung, 1997: Thermodynamic and optical properties of sea-salt aerosols. J. Geophys. Res., 102, 23 269–23 276.

Tang, I. N., and H. R. Munkelwitz, 1994: Water activities, densities, and refractive indices of aqueous sulfates and sodium nitrate droplets of atmospheric importance. *J. Geophys. Res.*, **99**, 18 801–18 808.

Veefkind, J. P., Aben, I., McMullan, K., Förster, H., de Vries, J., Otter, G., Claas, J., Eskes, H. J., de Haan, J. F., Kleipool, Q., van Weele, M., Hasekamp, O., Hoogeveen, R., Landgraf, J., Snel, R., Tol, P., Ingmann, P., Voors, R., Kruizinga, B., and Vink, R.: TROPOMI on the ESA Sentinel-5 Precursor: A GMES mission for global observations of the atmospheric composition for climate, air quality and ozone layer applications, Remote Sens. Environ., 120, 70–83, 2012.

Volz, F. E. (1973). Infrared optical constants of ammonium sulfate, Sahara dust, volcanic pumice, and flyash. Applied Optics, 12(3), 564-568.

Wang, C., Yuan, B., Wu, C., Wang, S. et al..: Measurements of higher alkanes using NO+ chemical ionization in PTR-ToF-MS: important contributions of higher alkanes to secondary organic aerosols in China, Atmos. Chem. Phys., 20, 14123–14138, https://doi.org/10.5194/acp-20-14123-2020, 2020.

Table S1 List of AMIP Experiments

Experiments*	Resolution over CONUS	Emissions and chemistry	Dry deposition	Physical climate
AM4.1 (LM4.1)	100 km	-CEDS v2017-05-18 -GFED4s	Prescribed monthly climatology	Zhao et al., 2018 Horowitz et al., 2020
AM4VR (LM4.0)	13 km	-CEDS v2021-04-21 -GFED4s with revised NMVOCs, injection height, and NO_y partitioning - Revised interactive BVOCs and SOA - Revised heterogeneous chemistry - Retuned interactive dust emissions	Interactive, calculated in the dynamic vegetation land model	Retuned moist physics parameterization (Sect. 2.2); ε_1 = 0.5 or 0.6 km^{-1}
C96 (LM4.0)	100 km	Similar to AM4VR, with some changes in dust emission parameters (Table S2)	Same as AM4VR	Same as AM4.1
C384 (LM4.0)	25 km	Same as AM4VR	Same as AM4VR	Similar to AM4VR, ε_1 = 0.7 km^{-1}

*The simulation time periods are 1980-2014 for AM4.1, 1988-2020 for AM4VR and C96, and 2008-2015 for C384

Table S2 Dust emission parameters

Parameters	AM4.1/LM4.1	AM4VR/LM4.0	C96/LM4.0
Wind erosion threshold (m/s):			
Natural vegetation	1	1	1
Secondary vegetation	1	1	1
Croplands	8	6	6
Pastures	6	4	4
Soil wetness threshold (top 15cm soil layers)	0.3	0.3	0.3
Scaling of the threshold wind velocity with soil moisture?	No	No	No
LAI threshold	0.1	0.2	0.35
SAI threshold	0.01	0.015	0.05
Snow cover threshold (kg/m^2)	0.01	0.01	0.01
Soil iceness	0.025	0.025	0.025
Global Emission Factor C (mg s^{-2} m^{-5})*	1.5	2.5	2.2
Soil mass fraction**: 0.1-1 mm	0.05	0.05	0.05
1-2 mm	0.15	0.15	0.15
2-3 mm	0.3	0.3	0.3
3-6 mm	0.27	0.27	0.27
6-10 mm	0.23	0.23	0.23

*Ginoux et al. (2001) and Evan et al. (2016) used 1.0 mg s^{-2} m^{-5}.

**Ginoux et al. (2001) and Evan et al. (2016) used 10% of clay and 22.5% for the other four bins.

(a) AM4.1

(b) AM4VR

0   500   1000   1500   2000   2500   3000
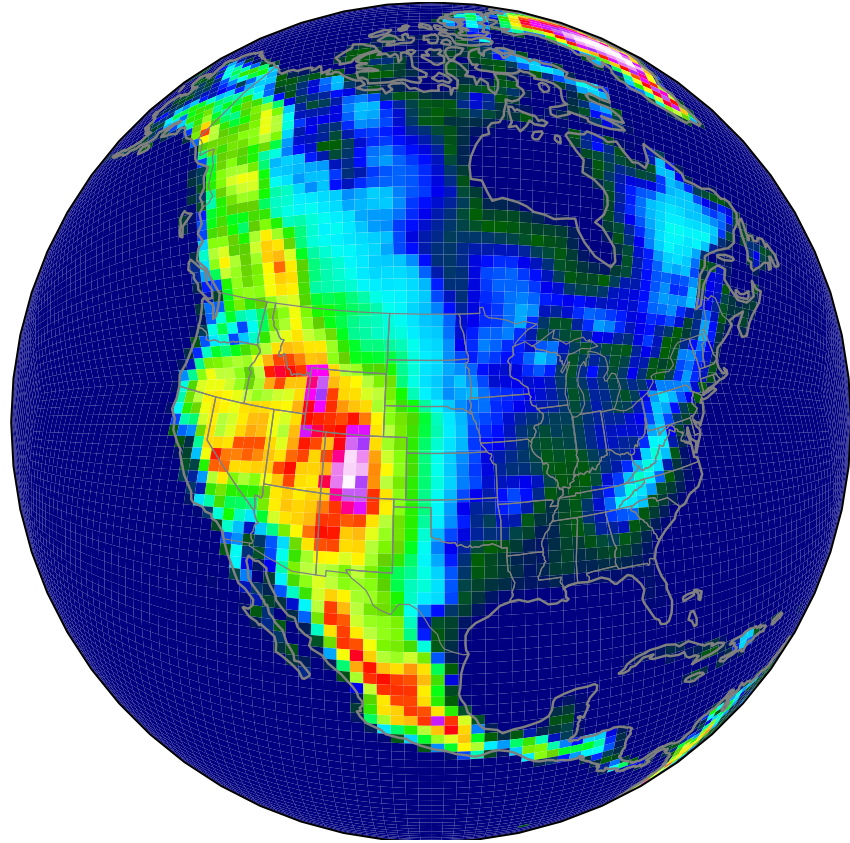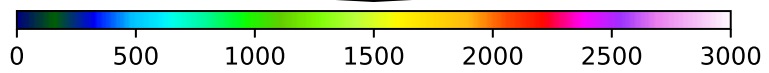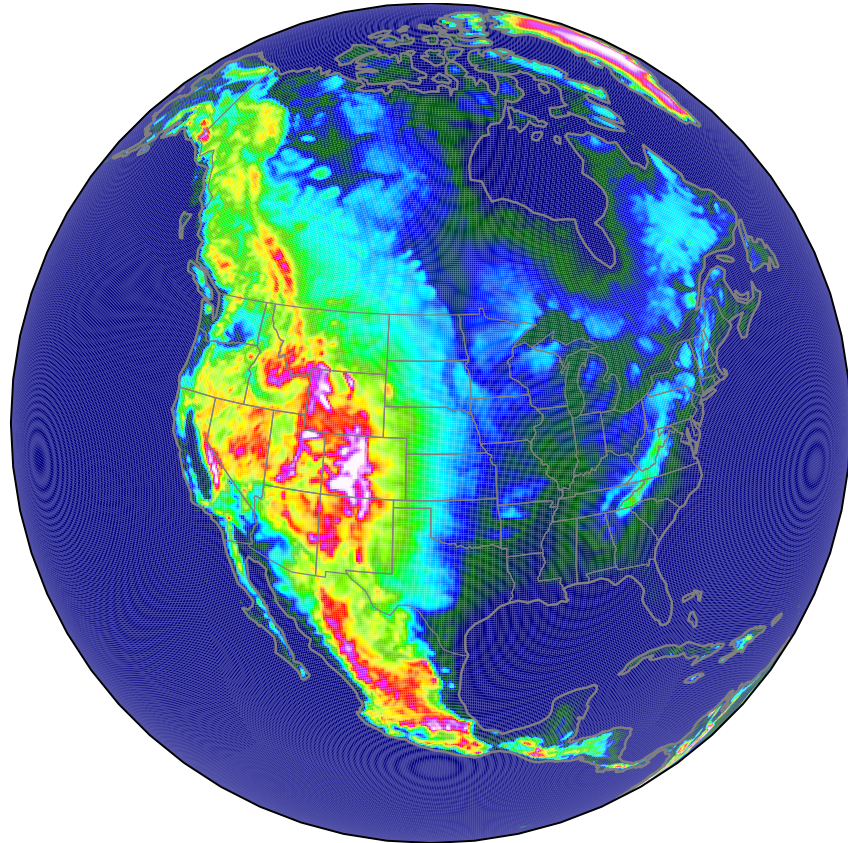
Figure S1. Comparison of surface elevation on the native cubed-sphere grid of AM4.1 (100km) versus AM4VR (13 km).
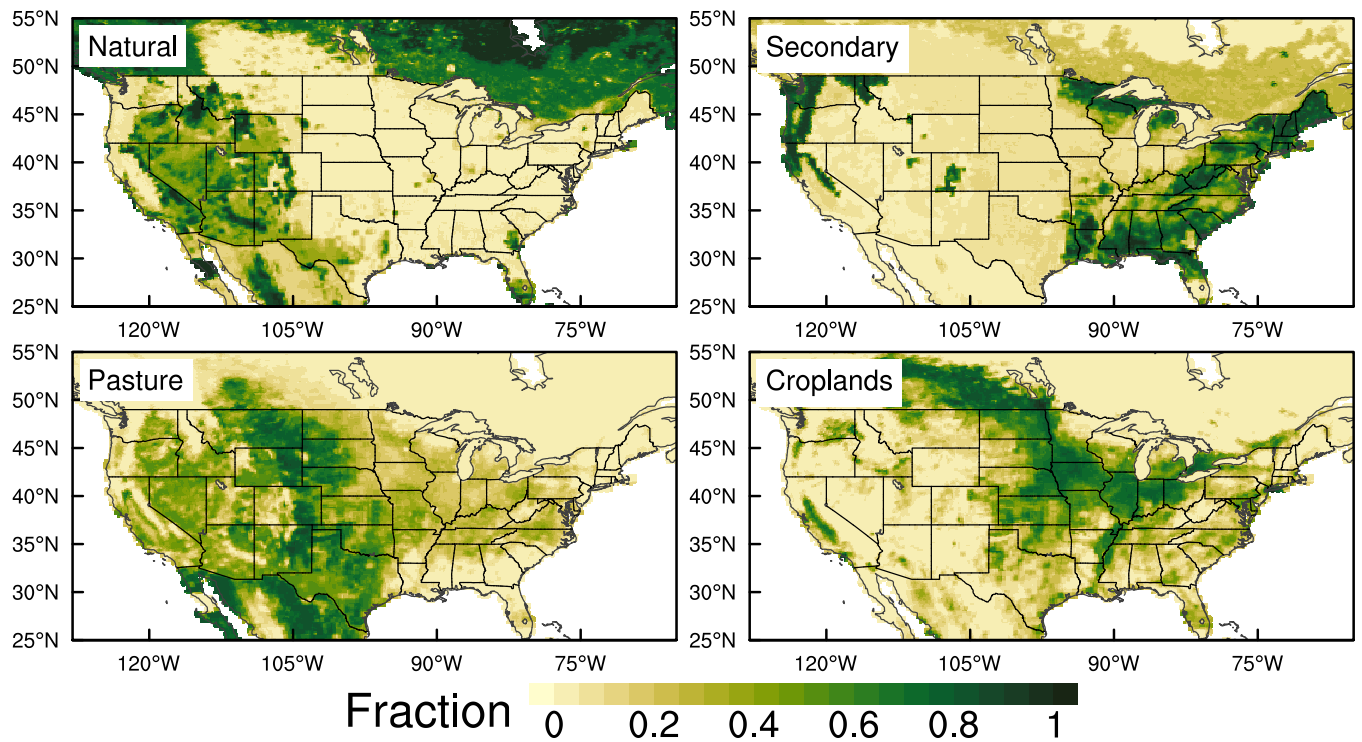
Figure S2. Fraction of the four land use categories in each grid cell: Natural forests (lands undisturbed by human activities), secondary vegetation (lands harvested at least once, including managed forests and abandoned cropland and pasture), pastures, and croplands. Results are shown over the CONUS domain from AM4VR AMIP simulation for 1990-2020.
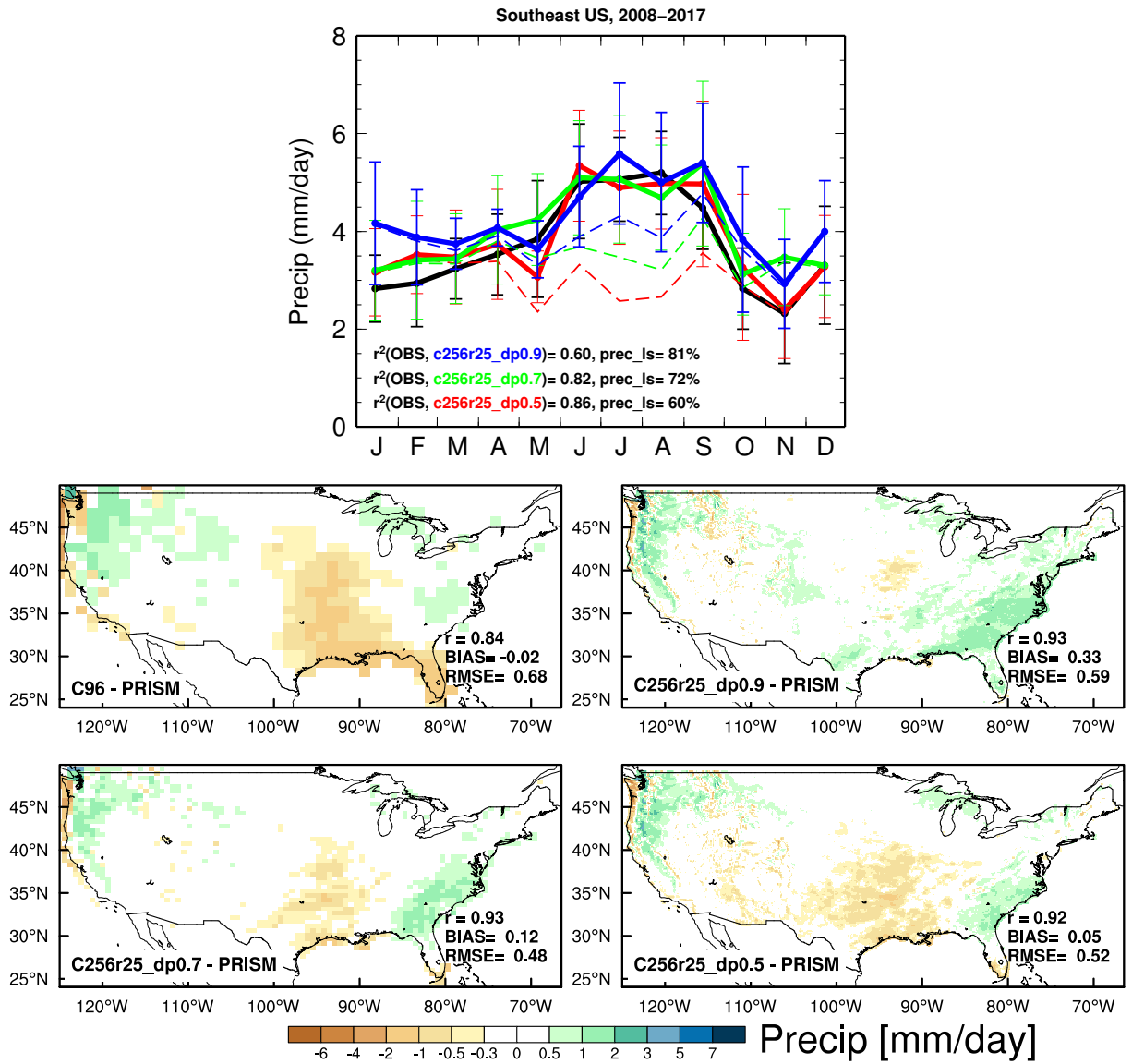
Figure S3. The top panel shows seasonal cycle of precipitation (mm day^{-1}) in the Southeast US (25-40N, 90-75W) for 2008-2017 from PRISM observations (black) and initial AM4VR AMIP simulations with changes in the deep plume lateral mixing rate: $\epsilon_1 = 0.9$ km^{-1} (blue), $\epsilon_1 = 0.7$ km^{-1} (green), and $\epsilon_1 = 0.5$ km^{-1}(red). Correlatons between observed and simulated total precipitation as well as the percentage of large scale prepication (dashed lines) for JJAS are reported. The bottom maps display bias in simulated US annual mean precipitation relative to PRISM observations.
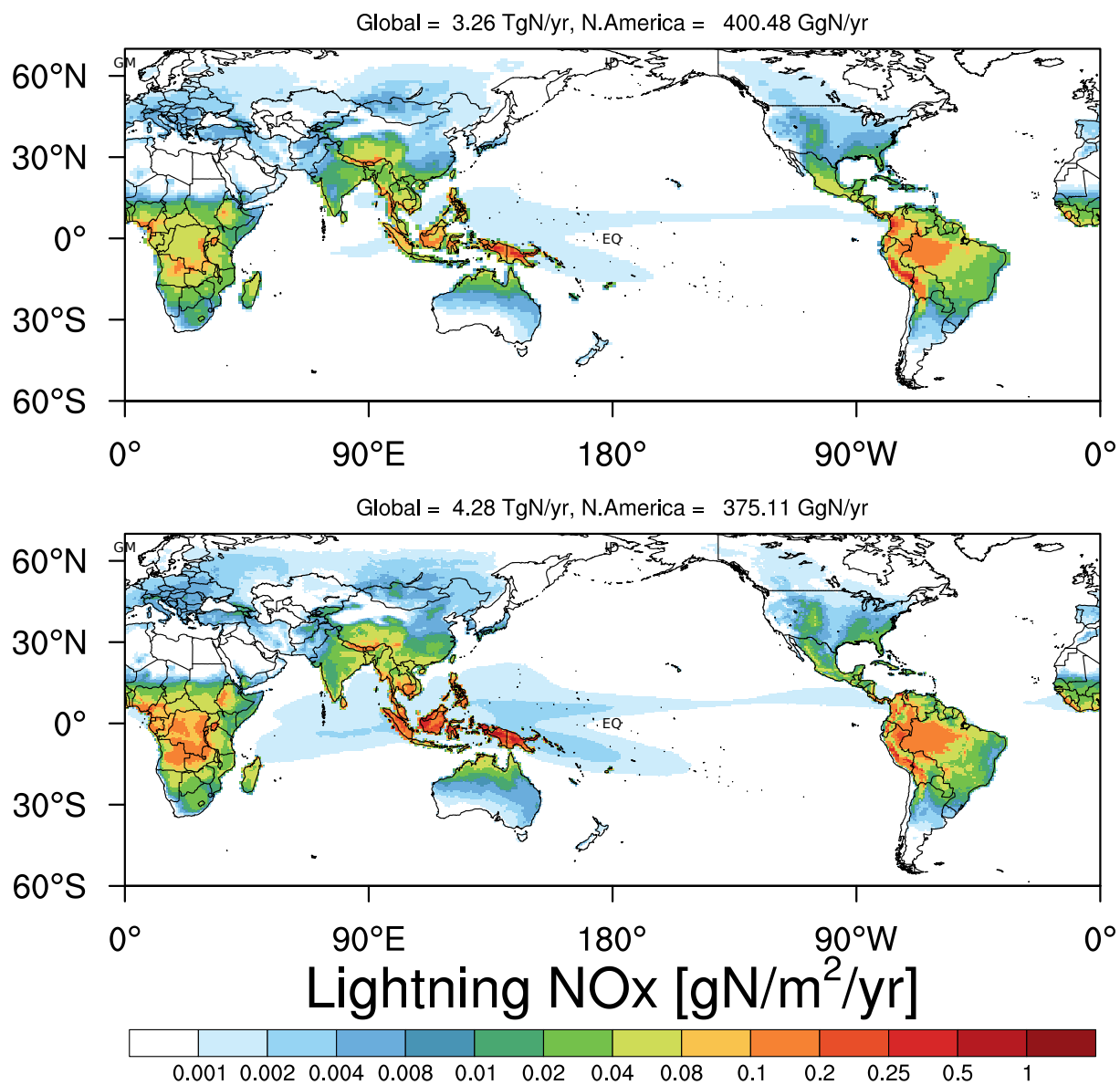
Figure S4. Lightning NO emissions computed in AM4.1 (top) and AM4VR (bottom) AMIP simulations. Global and North American (0-80N, 225-305E) totals are reported.
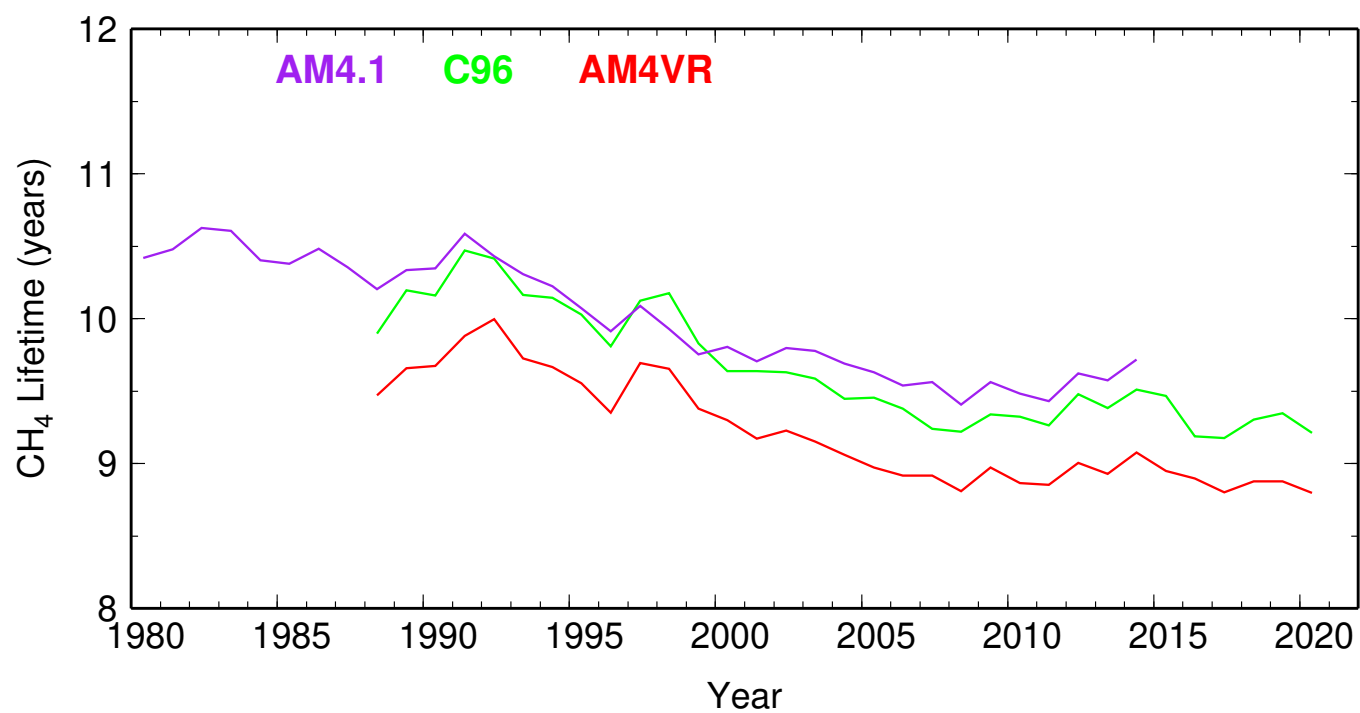
Figure S5. Methane lifetime against loss by reaction with tropospheric OH from AM4.1, C96 and AM4VR AMIP simulations.
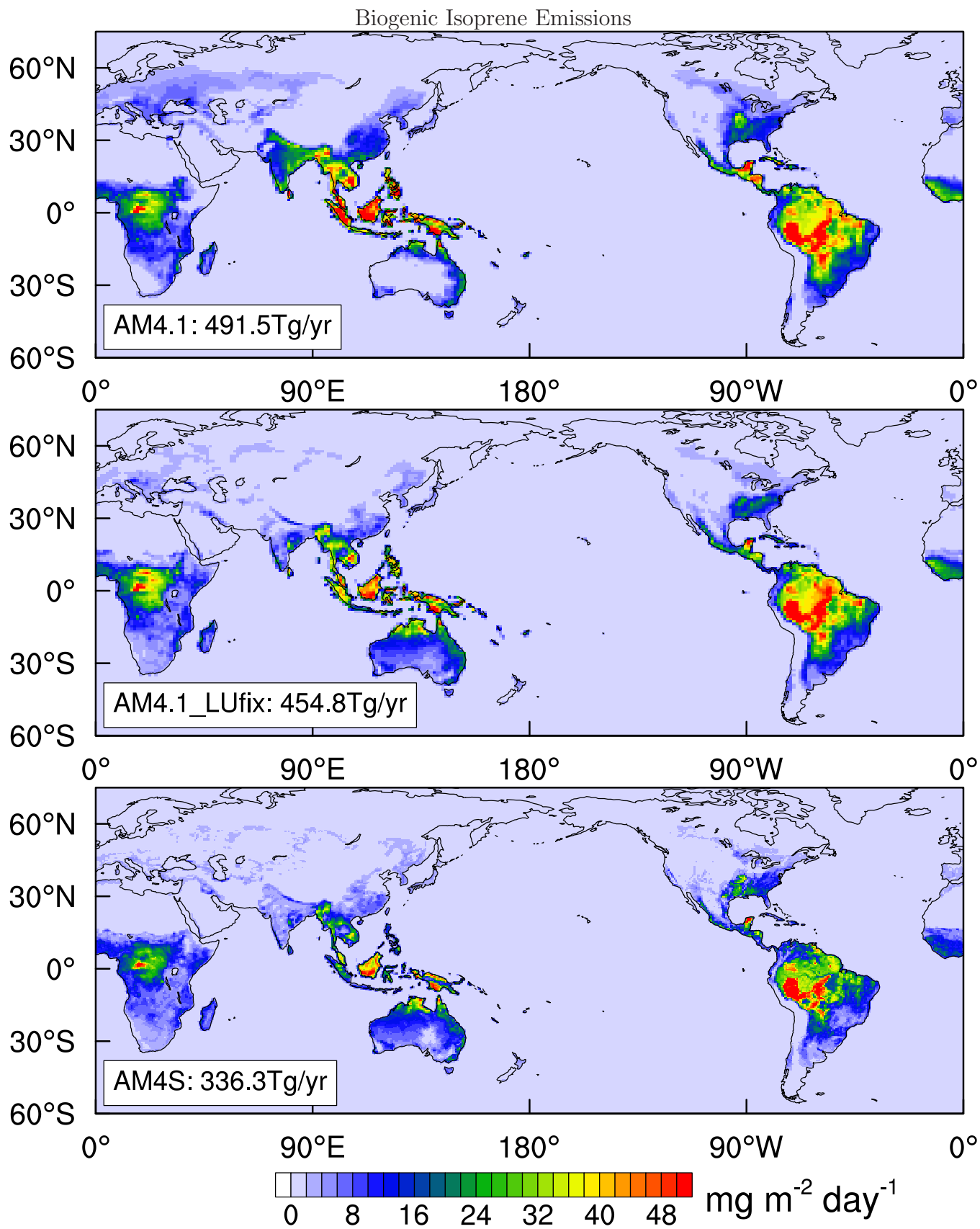
Figure S6. Global distribution of annual mean biogenic isoprene emission fluxes computed in the AMIP simulations (2000-2014) with AM4.1 in the CMIP6 confituration, AM4.1 with the landuse fix, and AM4VR with updates described in the text. Unit: mg(C5H8)/m^2/day

Biogenic Monoterpene Emissions

AM4.1: 132.1 +/- 2.6Tg/yr

AM4VR: 95.8 +/- 1.5Tg/yr

Monoterpenes [mg m^{-2} day^{-1}], ANN

0.1 0.5 1 1.5 3 4 5 8 12 16
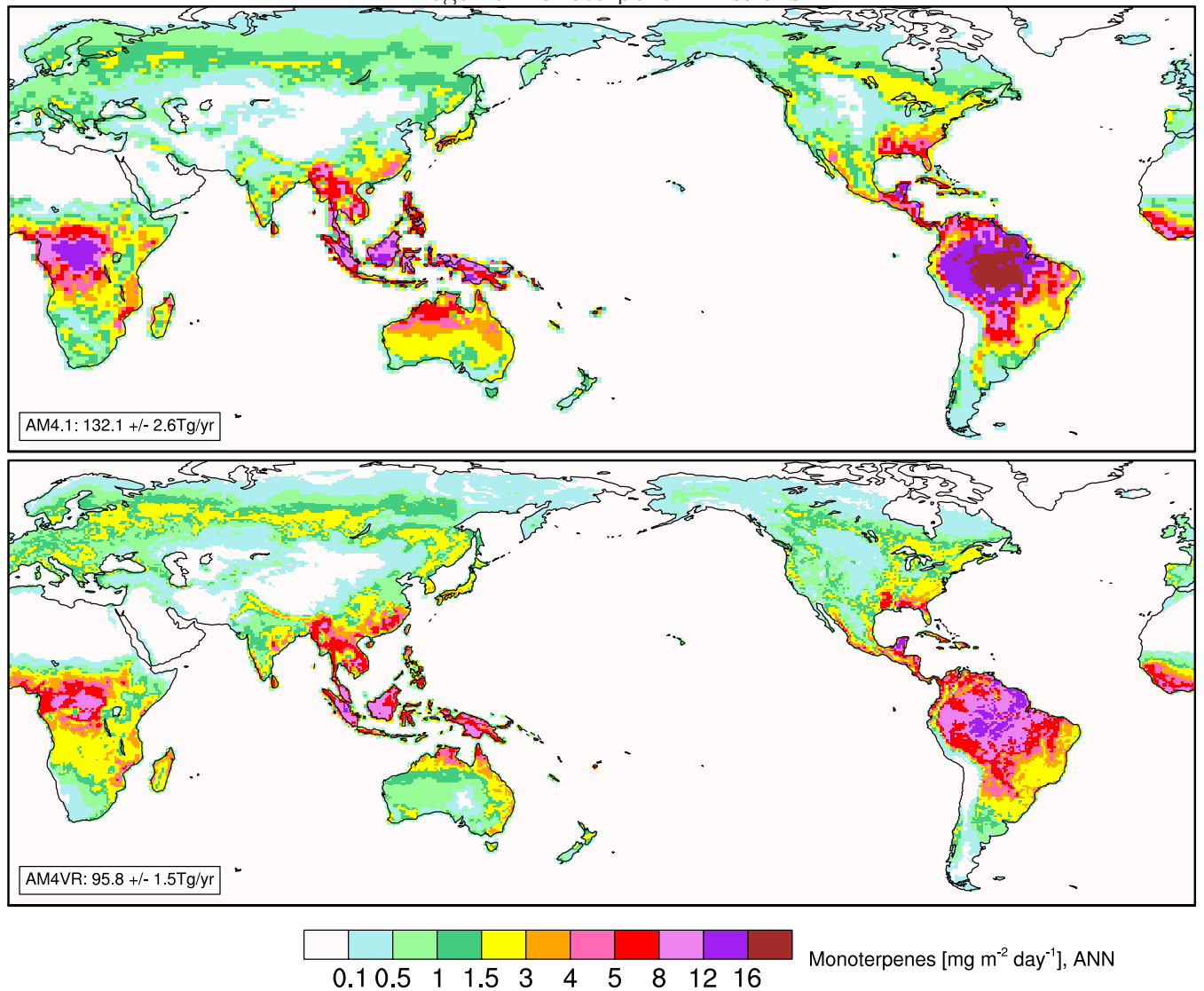
Figure S7. Global distribution of annual mean biogenic monoterpenes emision fluxes computed in the AMIP simulations (2000-2014) with AM4.1 and AM4VR. Unit: mg(C10H16)/m^2/day.

Other BVOCs

AM4.1: 113.0 +/- 0.0 Tg(C)/yr

AM4S: 111.4 +/- 3.5 Tg(C)/yr

Ton(C)/km²/yr

0.1 0.2 0.5 1 1.4 1.8 2.2 2.5 3 5
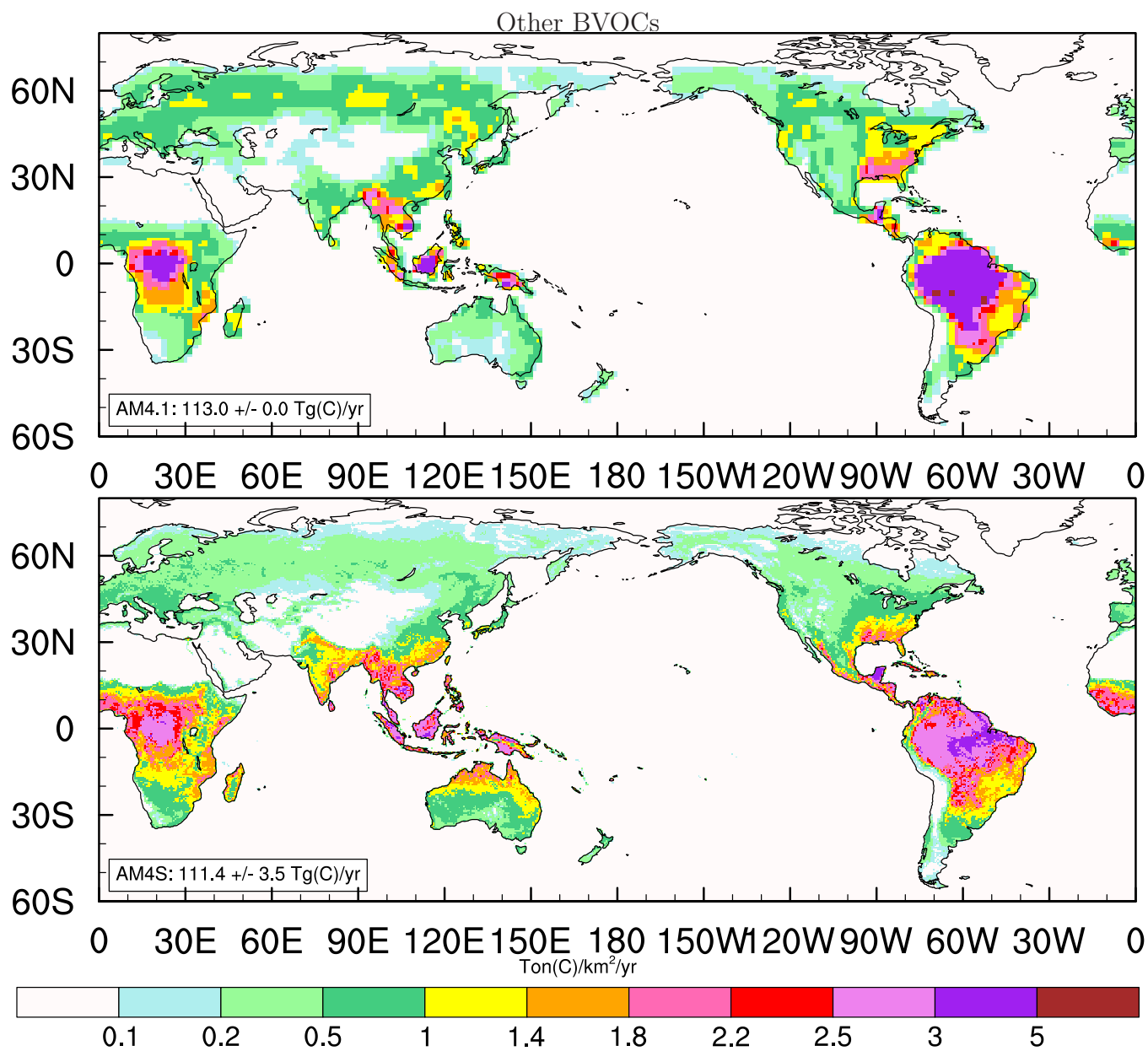
Figure S8. Global distribution of annual mean emission fluxes (Ton(C)/km²/yr) for other BVOCs prescribed in AM4.1 (fixed-2000) and AM4VR (interannually varying during 2000-2020).
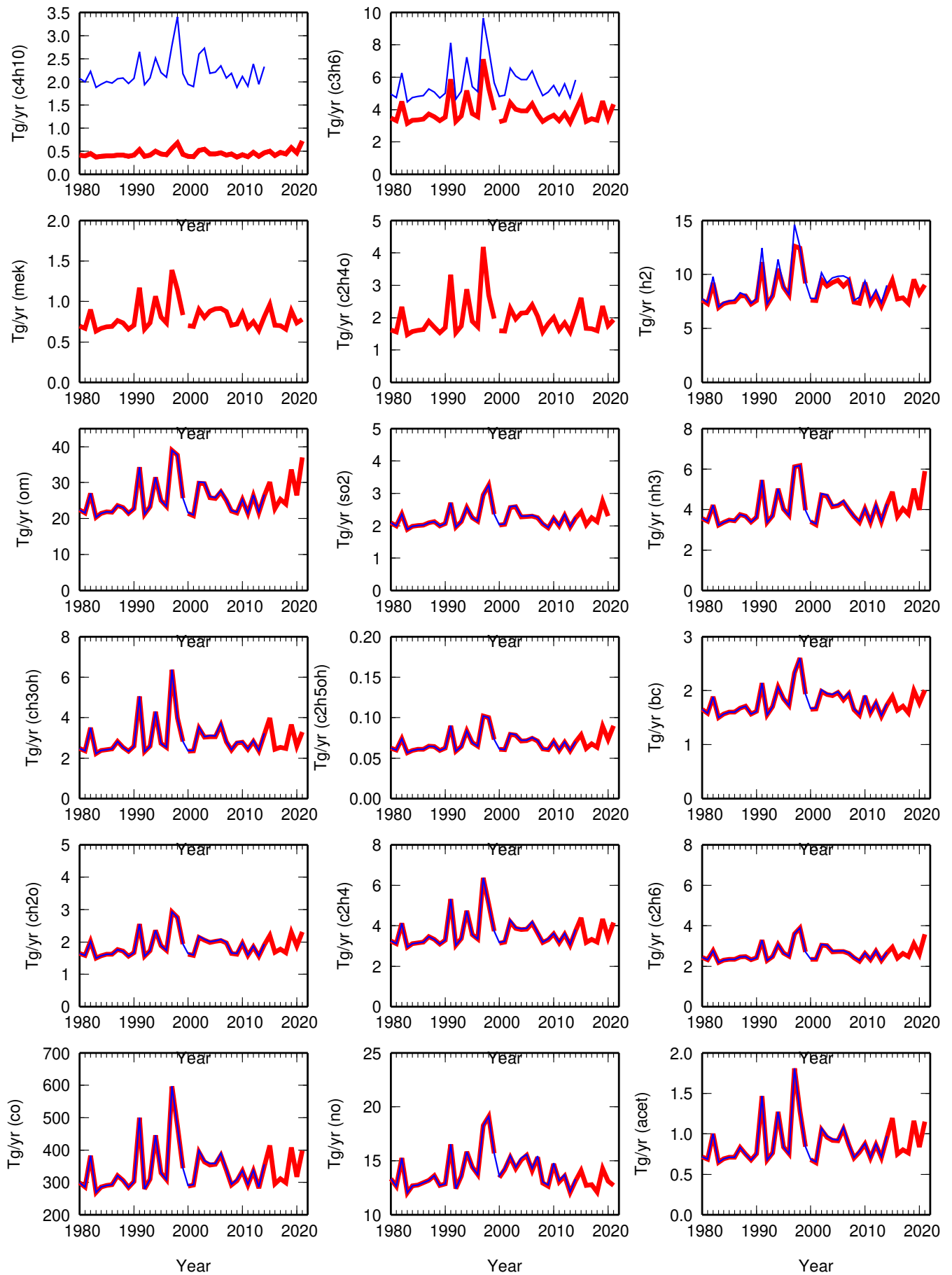
Figure S9. Time series of global total biomass burning emissions for AM4.1 (blue lines; 1980-2014) and AM4VR (red lines; 1980-2020). AM4VR accounts for biomass burning emissions of MEK and C2H4O and includes a correction to C4H10 and C3H6 emissions (see Text S4).
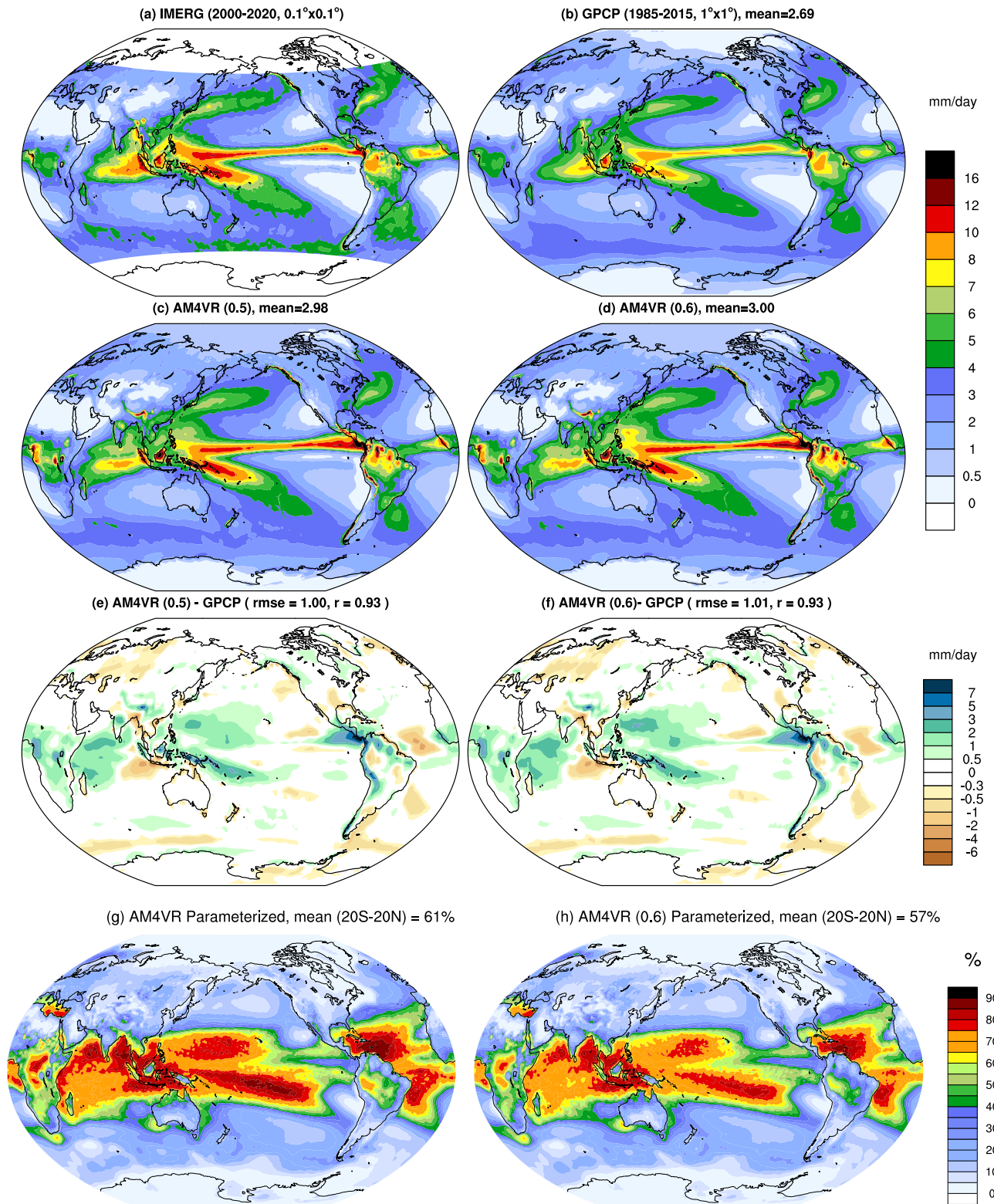
Figure S10. (a-d) Long-term annual mean precipitation (mm day^{-1}) from observation-based estimates from GPCP (1°, 1985-2015) and IMERG (0.1^o, 2000-2020) and from the two AM4VR (regridded to 50 km globally) AMIP simulations for 1990-2020 with $\epsilon_1 = 0.5$ and $= 0.6$ km^{-1}, respectively. (e-f) Differences between simulated results and GPCP estimates. (g-h) Fraction of parameterized deep convective precipitation.
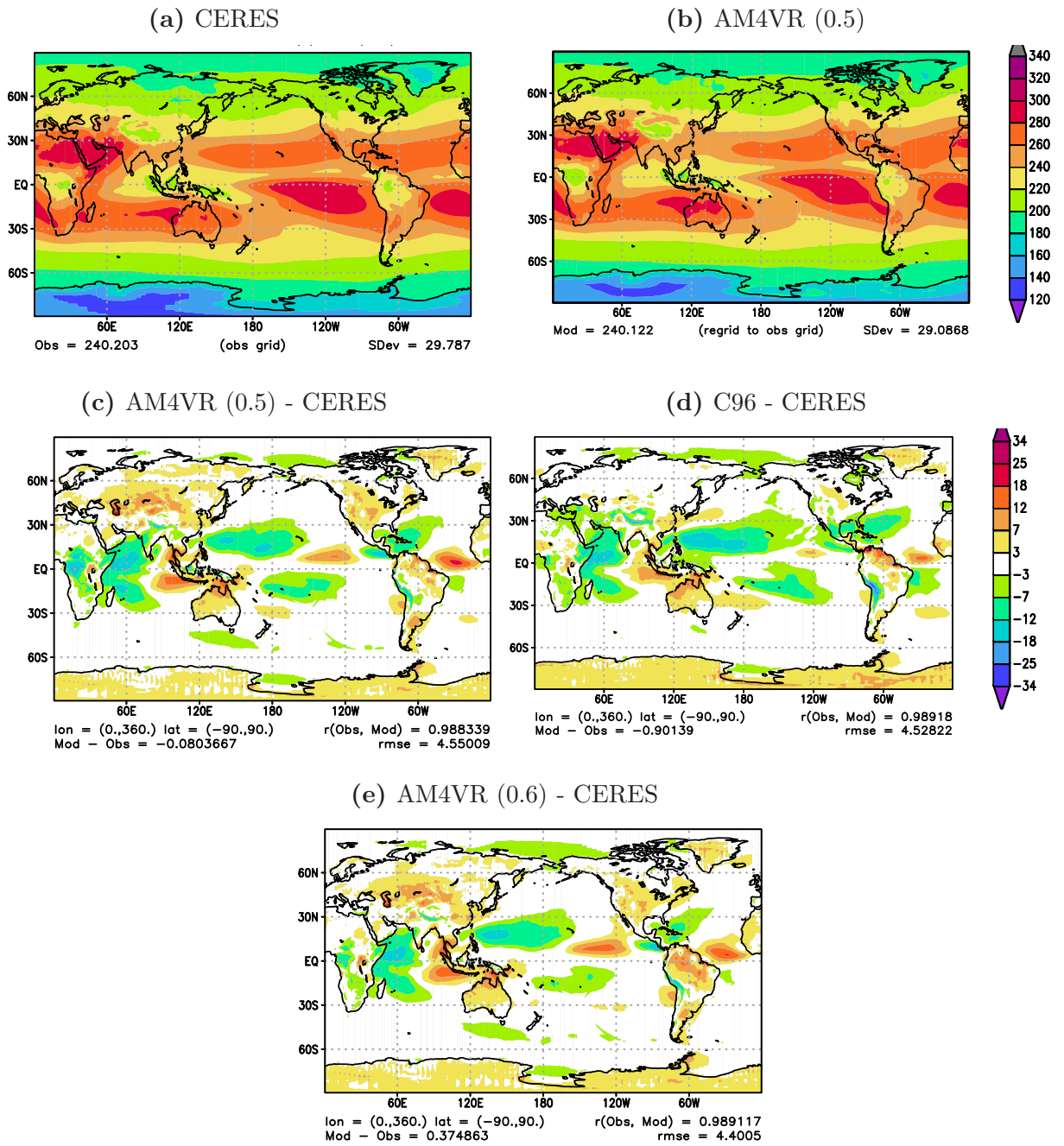
Figure S11. Long-term annual mean TOA outgoing longwave radiative flux (W/m²) from (a) observational estimate based on CERES-EBAF-ed4.1 (2001-2015), (b) AM4VR AMIP simulation (1990-2020) ($\epsilon_1 = 0.5$ km^{-1}), and (c-e) differences between observed and simulated values for AM4VR with $\epsilon_1 = 0.5$ km^{-1}, C96 with $\epsilon_1 = 0.9$ km^{-1}, and AM4VR with $\epsilon_1 = 0.6$ km^{-1}.

(a) CERES

(b) AM4VR (0.5)

(c) AM4VR (0.5) - CERES

(d) C96 - CERES

(e) AM4VR (0.6) - CERES
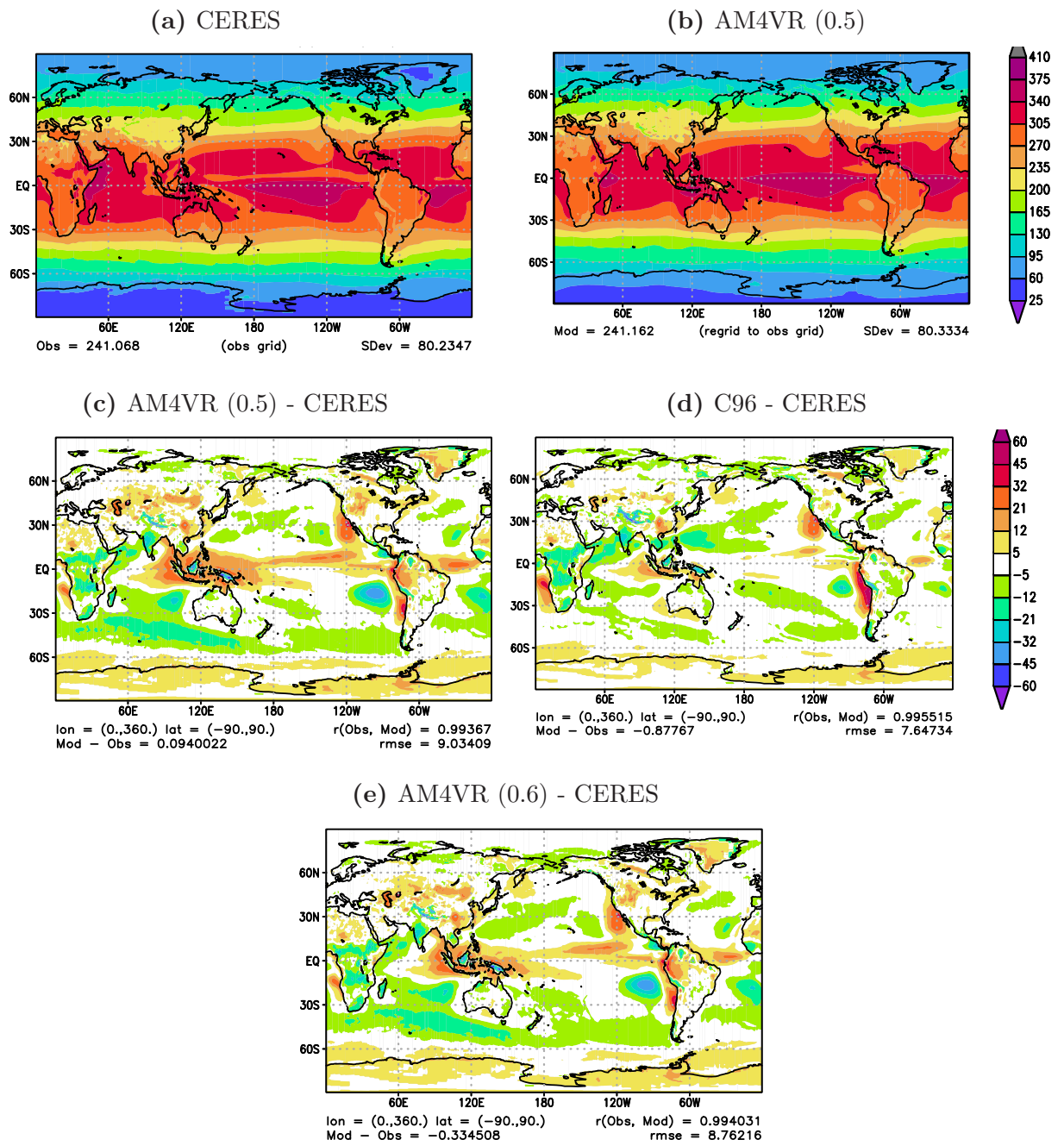
Figure S12. Same as Fig. S11 but for TOA net SW downward (absorption) radiative flux (W/m^2).

(a) CERES

(b) AM4VR (0.5)

Obs = −45.3939   (obs grid)   SDev = 20.3858

Mod = −47.2771   (regrid to obs grid)   SDev = 21.502

(c) AM4VR (0.5) - CERES

(d) C96 - CERES

lon = (0.,360.) lat = (−90.,90.)   r(Obs, Mod) = 0.907377
Mod − Obs = −1.88317   rmse = 9.2732

lon = (0.,360.) lat = (−90.,90.)   r(Obs, Mod) = 0.928295
Mod − Obs = −2.63885   rmse = 8.14995

(e) AM4VR (0.6) - CERES

lon = (0.,360.) lat = (−90.,90.)   r(Obs, Mod) = 0.909119
Mod − Obs = −2.16513   rmse = 9.21703
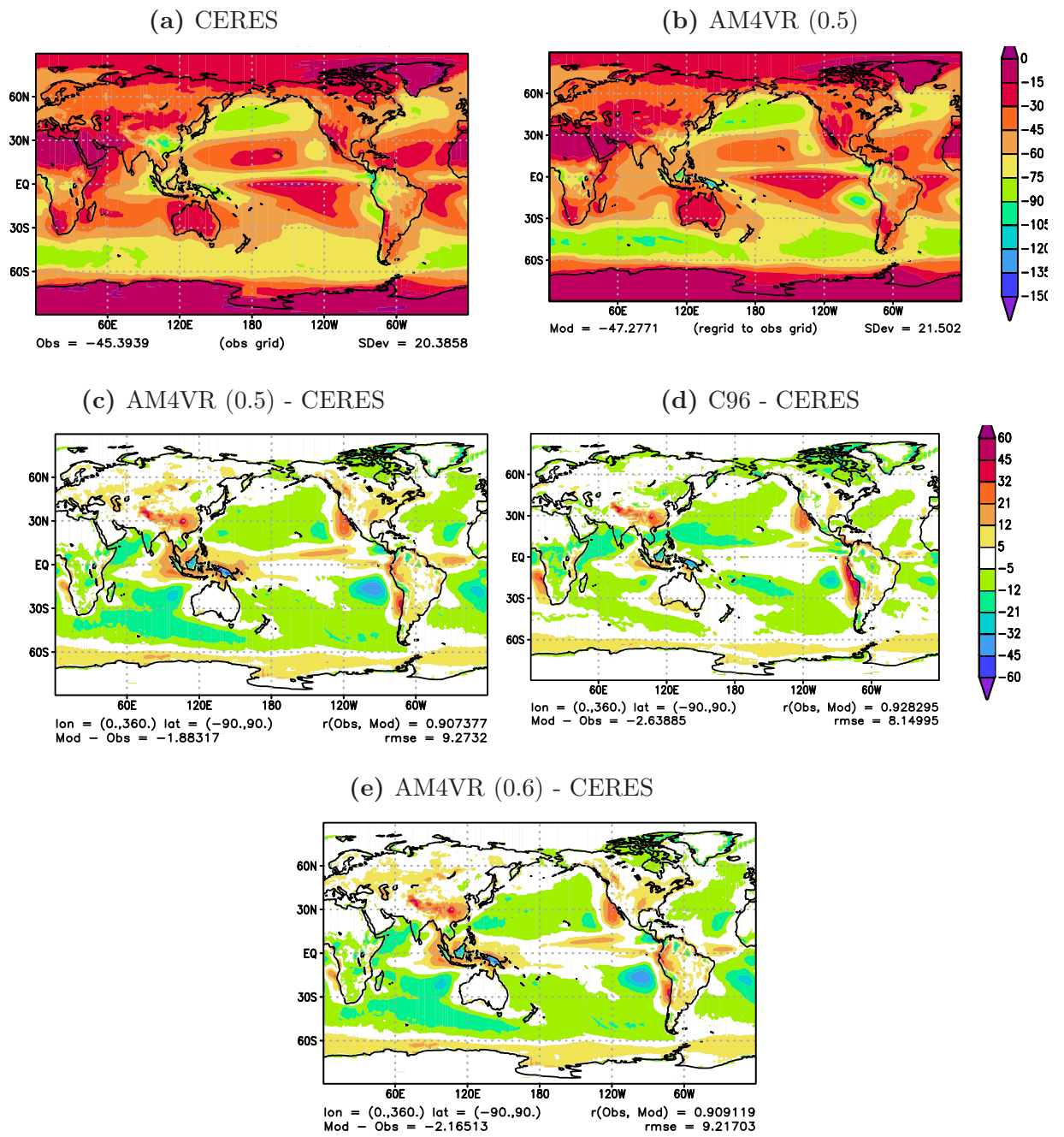
Figure S13. Same as Fig. S11 but for shortwave cloud radiative effects at TOA (W/m^2).
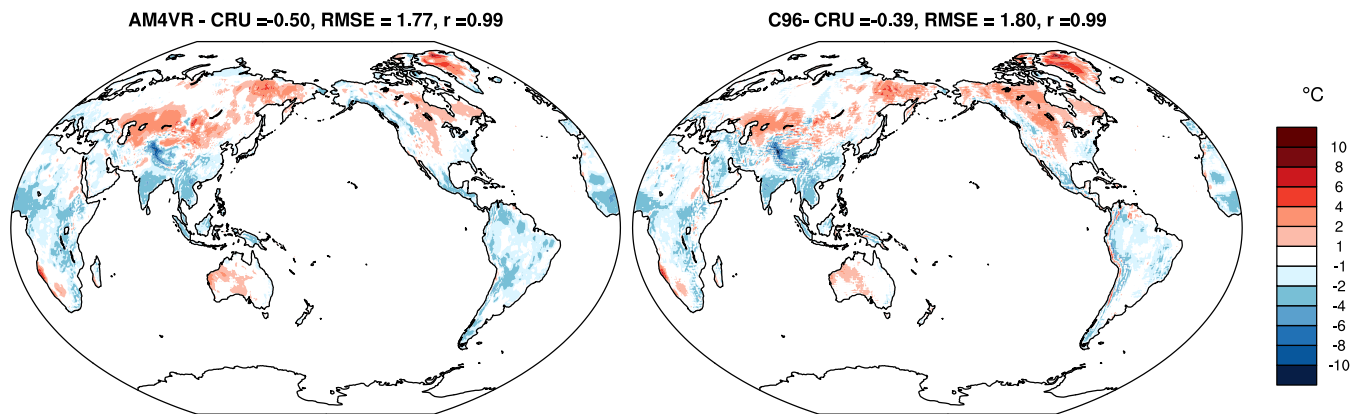
Figure S14. Model bias in long-term annual mean surface air temperature over land in comparison with observational estimates from CRU-v4.06.
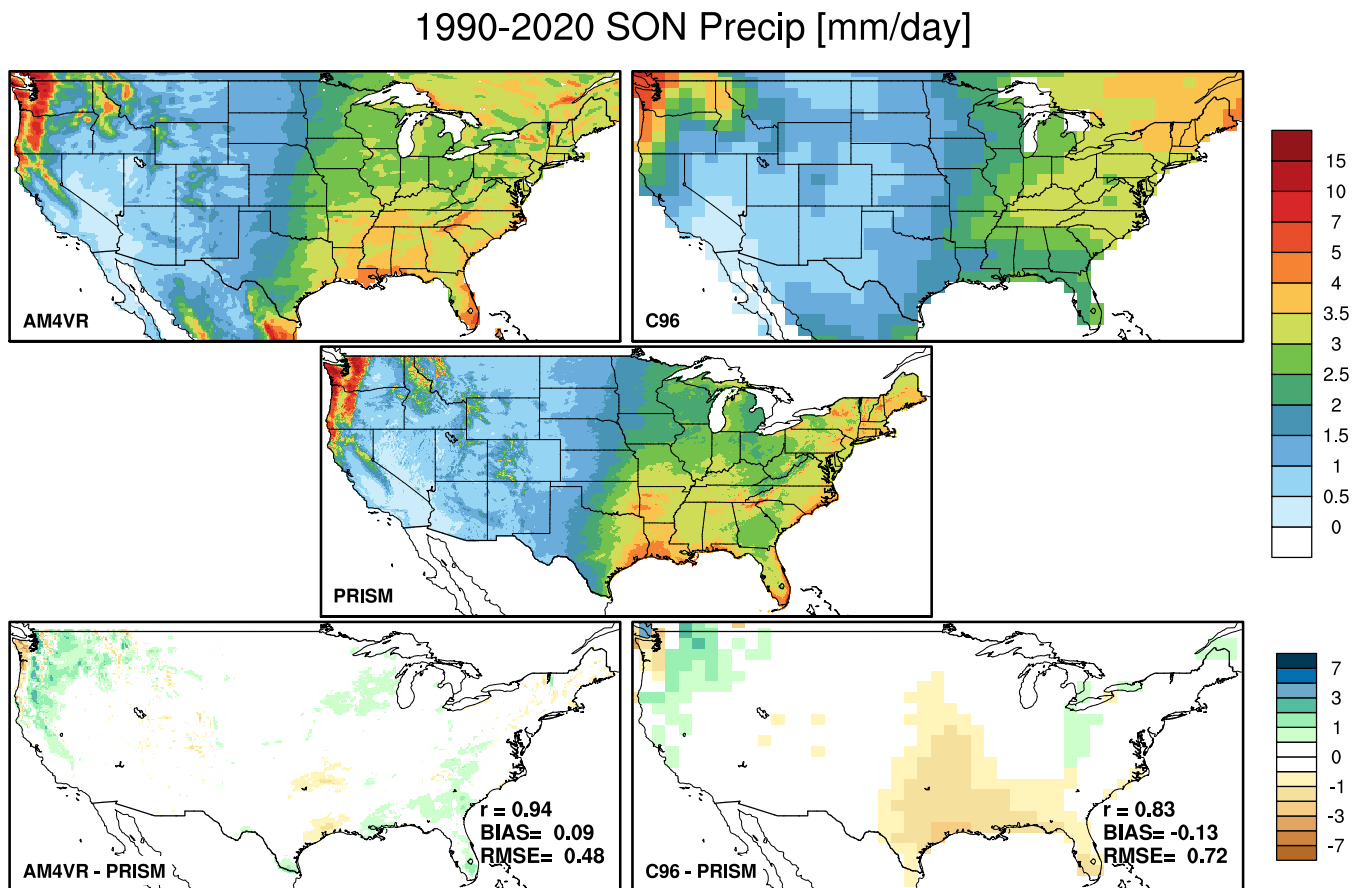

Figure S15. US SON mean precipitation from AM4VR (13 km, $\epsilon_1 = 0.6$ km^{-1}) and C96 (100 km, $\epsilon_1 = 0.9$ km^{-1}) AMIP simulations, PRISM observations (4 km), and differences between simulated and observed results.

1990-2020 DJF Precip [mm/day]
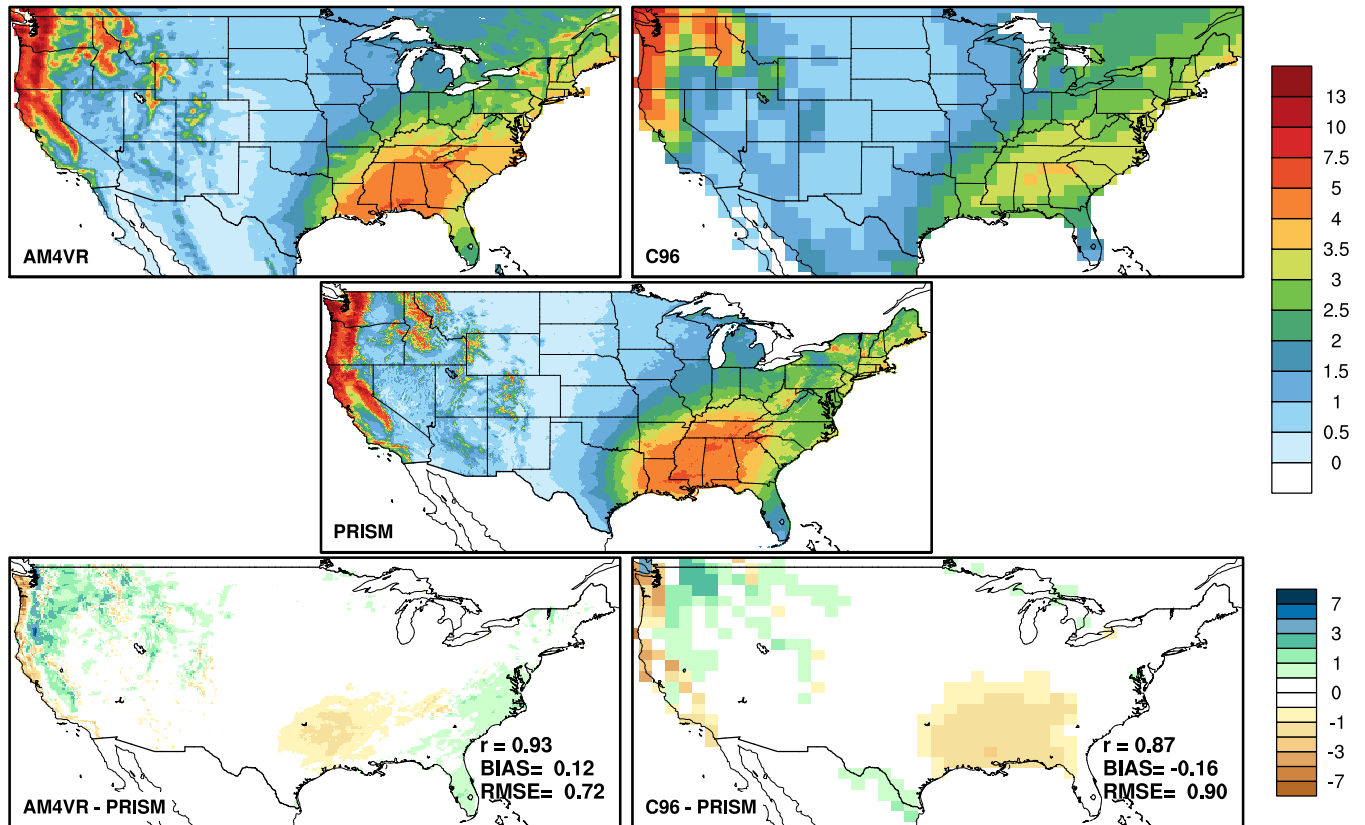
Figure S16. US DJF mean precipitation from AM4VR (13 km, $\epsilon_1 = 0.6$ km^{-1}) and C96 (100 km, $\epsilon_1 = 0.9$ km^{-1}) AMIP simulations, PRISM observations (4 km), and differences between observed and simulated results.
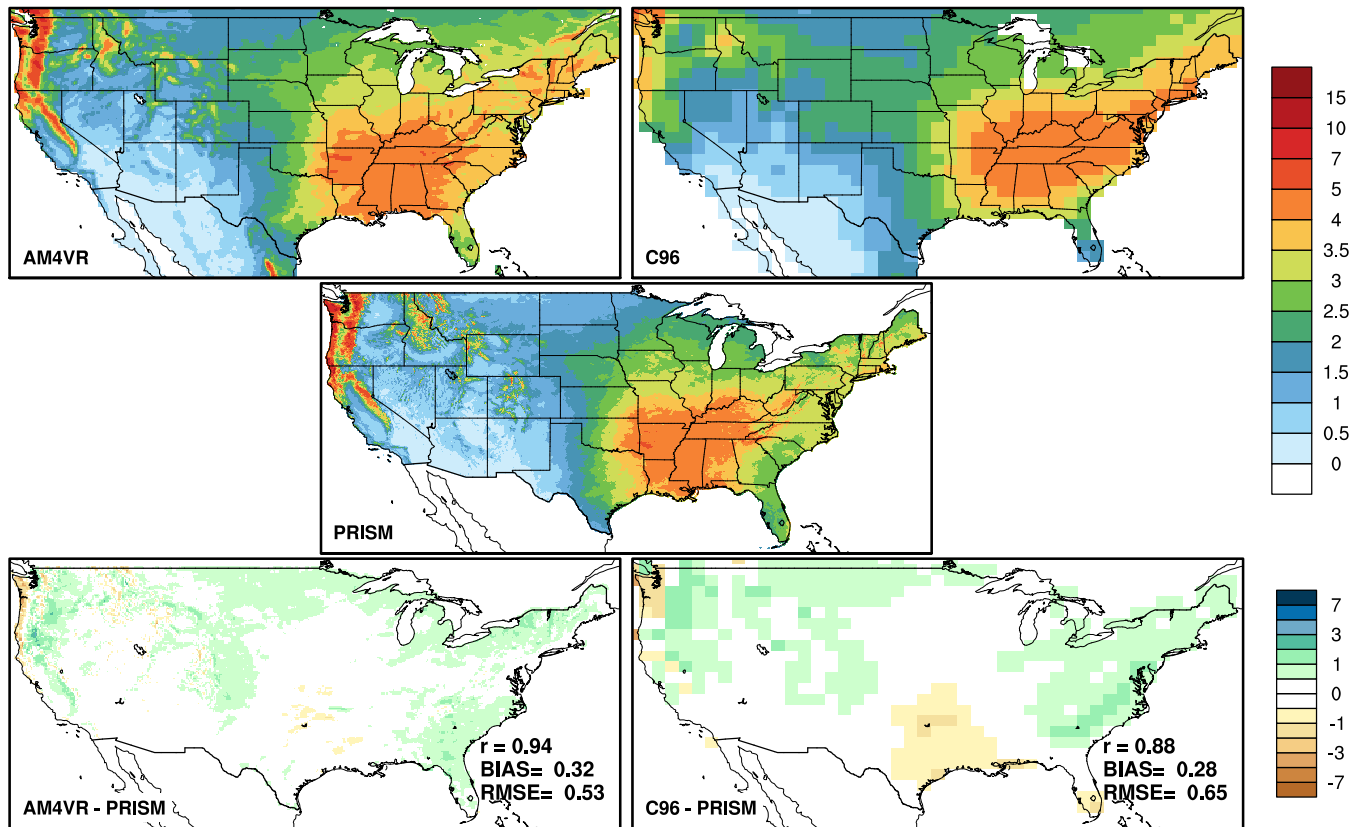
Figure S17. US MAM mean precipitation from AM4VR ($\epsilon_1 = 0.6$ km^{-1}) and C96 ($\epsilon_1 = 0.9$ km^{-1}) AMIP simulations, PRISM observations, and differences between observed and simulated results.
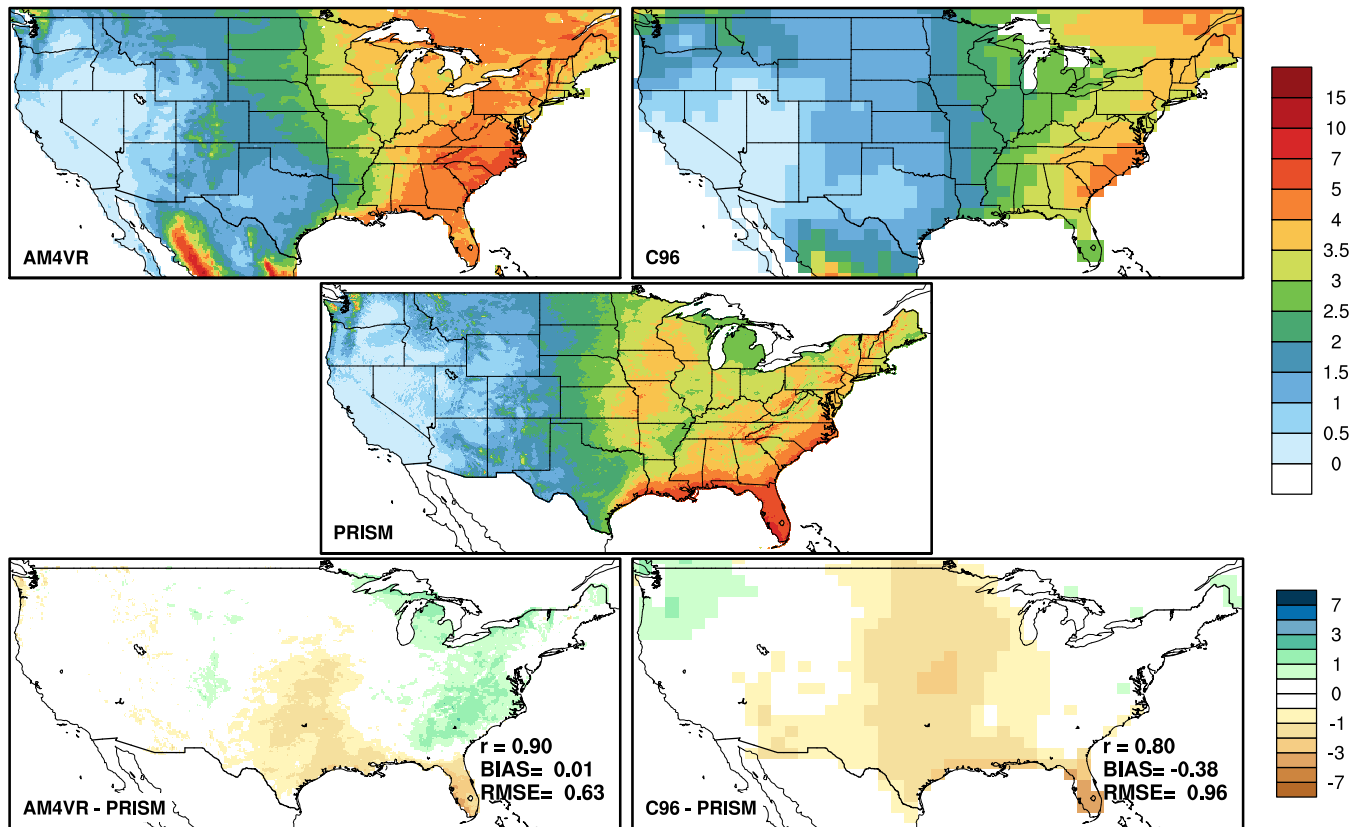
Figure S18. US JJAS mean precipitation from AM4VR ($\epsilon_1 = 0.6$ km^{-1}) and C96 ($\epsilon_1 = 0.9$ km^{-1}) AMIP simulations, PRISM observations, and differences between observed and simulated results.

JJAS effective white-sky (diffusive) land albedo, total
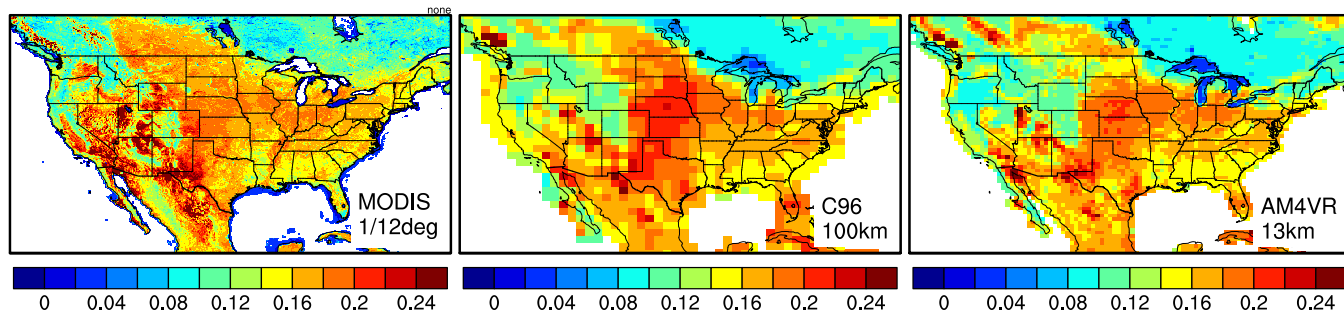
JJAS effective white-sky (diffusive) land albedo, vis
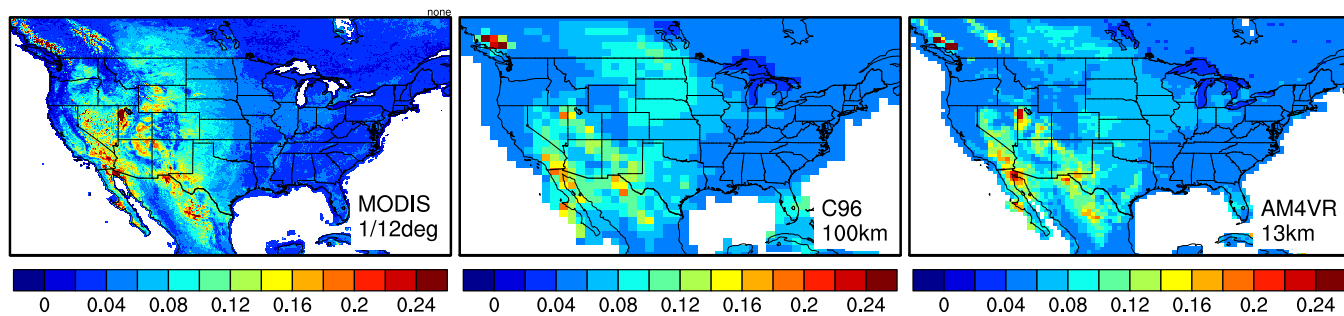
JJAS effective white-sky (diffusive) land albedo, nir
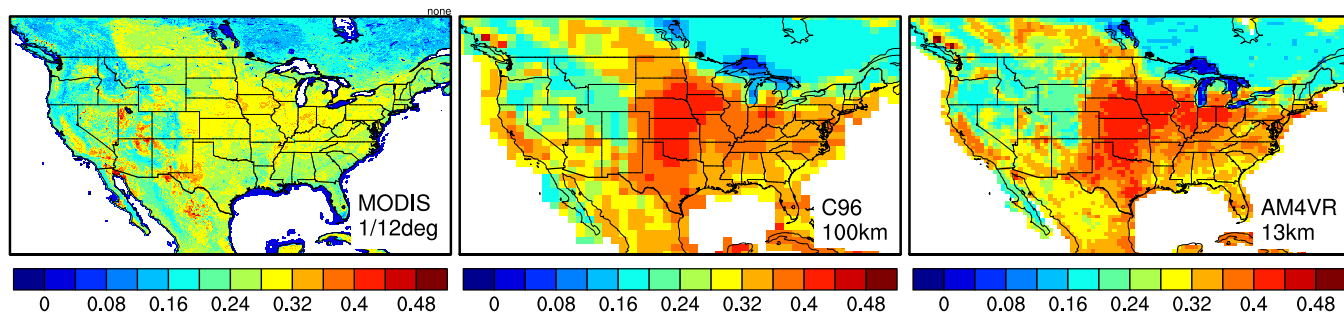
Figure S19. Maps of June-September average of effective white-sky (diffuse) land albedo derived from MODIS and from C96 and AM4VR AMIP simulations. Effective albedo is ratio of time averages of upward and downward shortwave radiation. Results are shown seperately for the total albedo, the visible (VIS) and near-infrared (NIR) albedo.

(a) AM4VR AMIP (2000-2014)
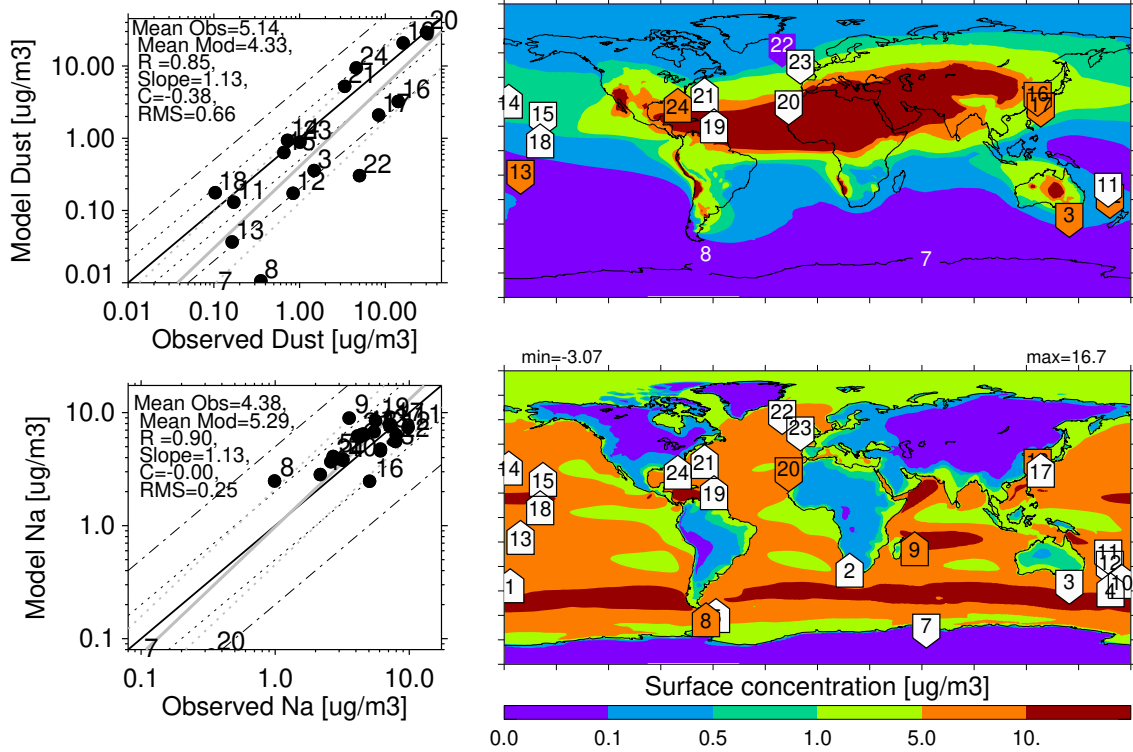
(b) C96 AMIP (2000-2014)
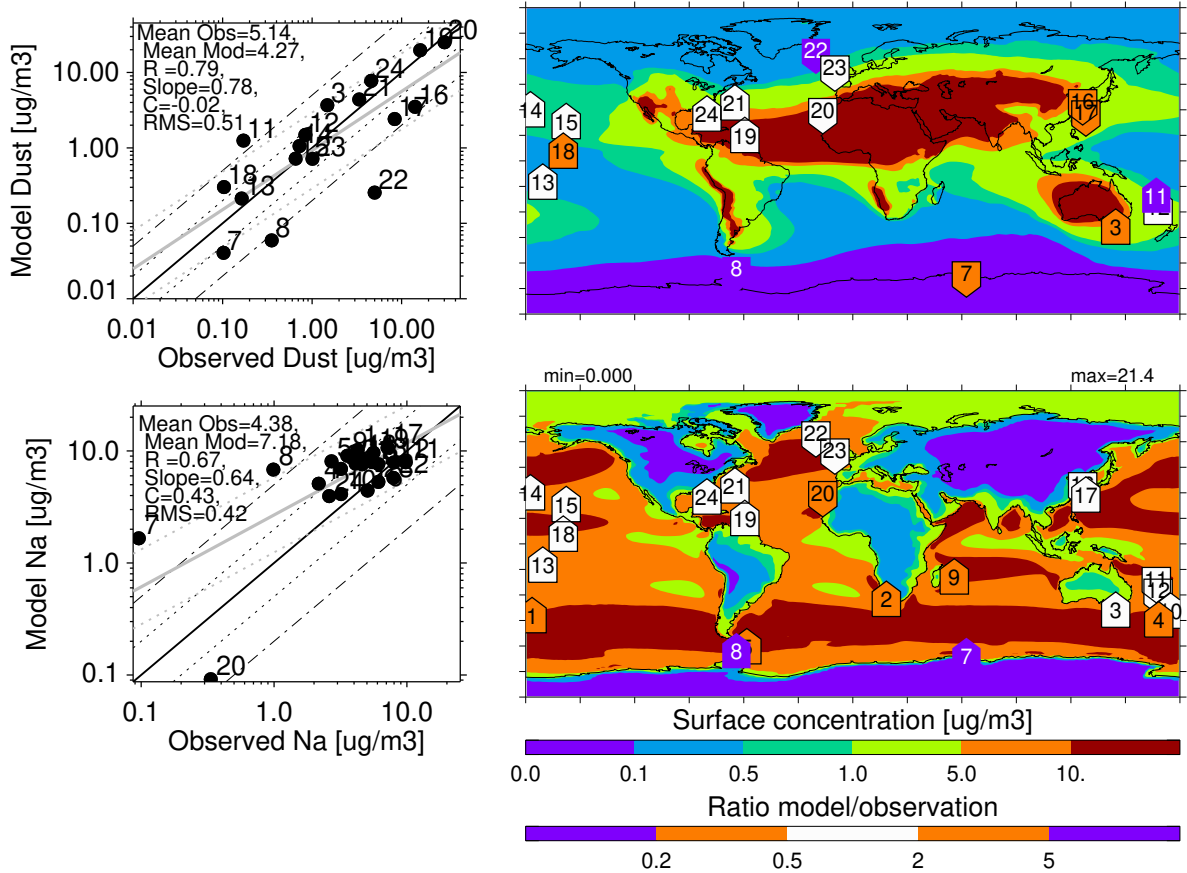
Figure S20. Comparison of simulated and observed (University of Miami) annual mean surface concentrations (μ m^{-3}) of (first row) dust and (second row) sea salt sodium at 28 locations. Shaded contours indicate simulated surface concentrations (top colorbar) and symbols indicate the ratio of simulated/observed concentrations (bottom colorbar, symbol points upwards if ratio greater than one, downwards if less than one).
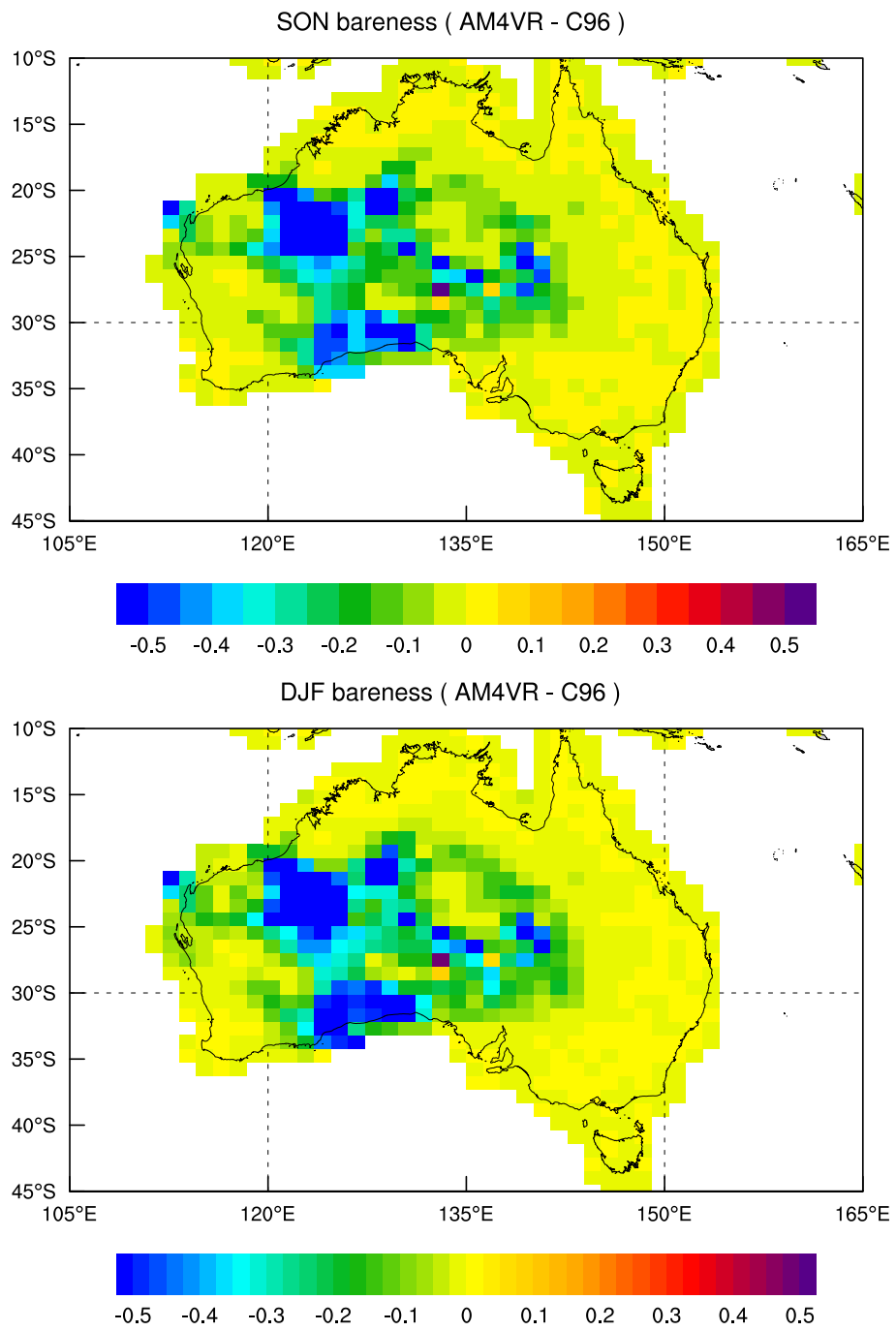
Figure S21. Difference between AM4VR and C96 simulated surface bareness over Australia in austrial spring (SON) and summer (DJF).
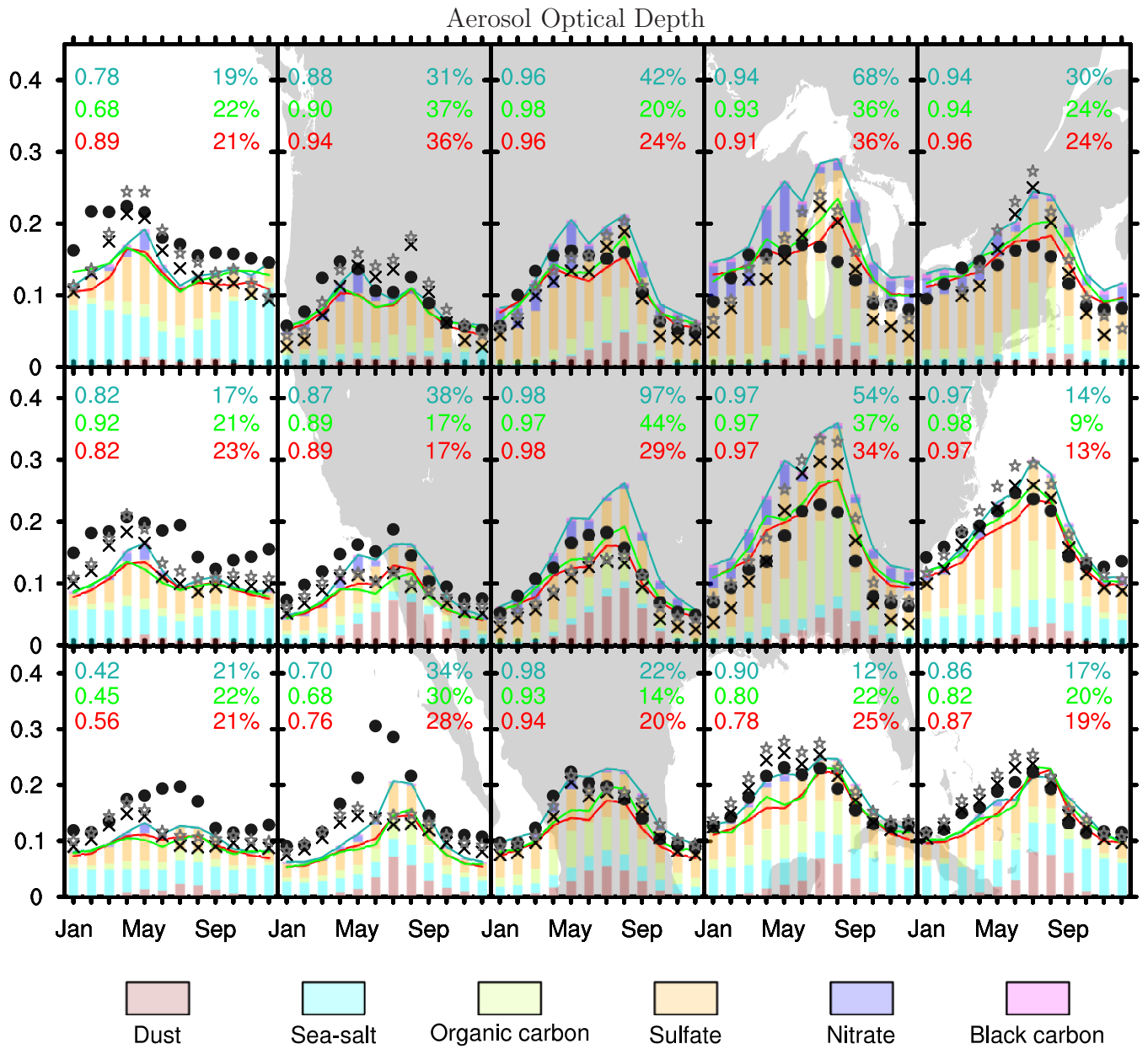
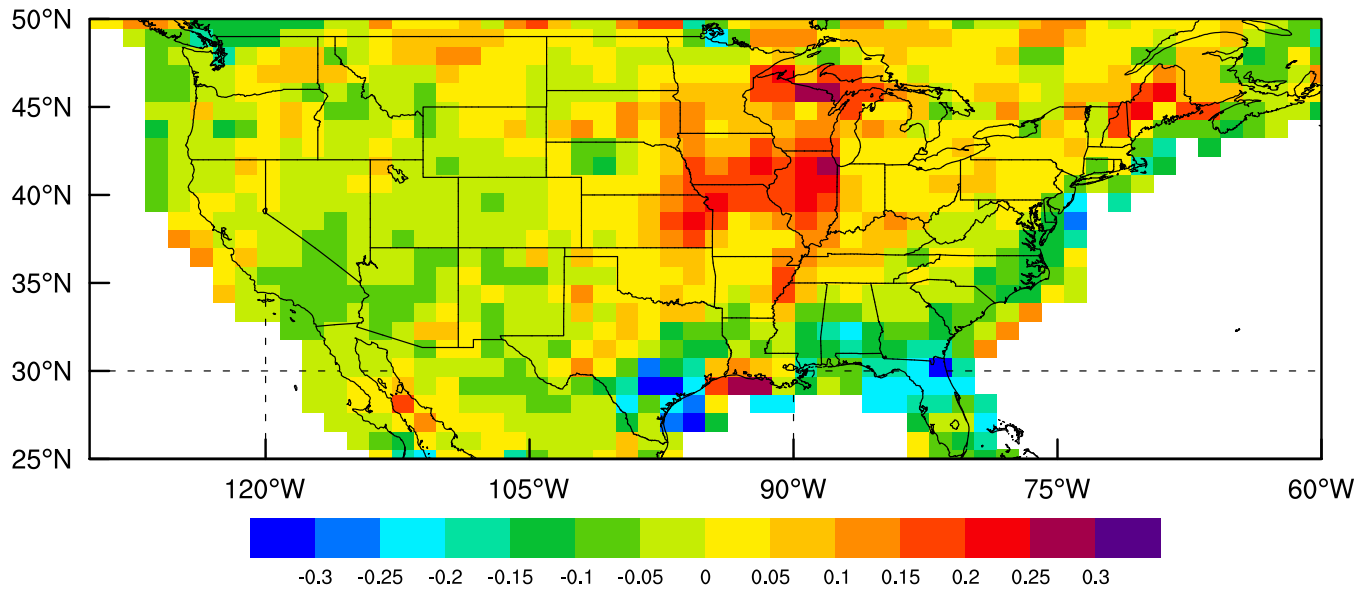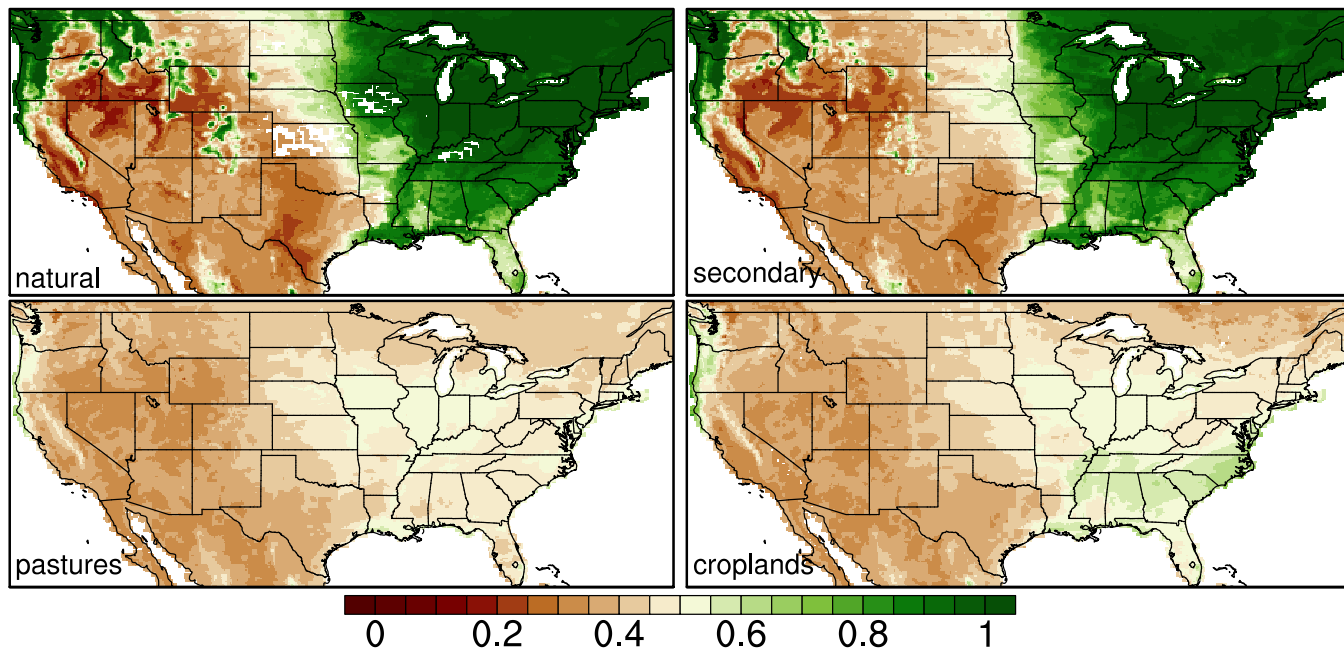Figure S22. As in Fig.16 in the main article but with the vertical bars showing aerosol components in AM4.1.
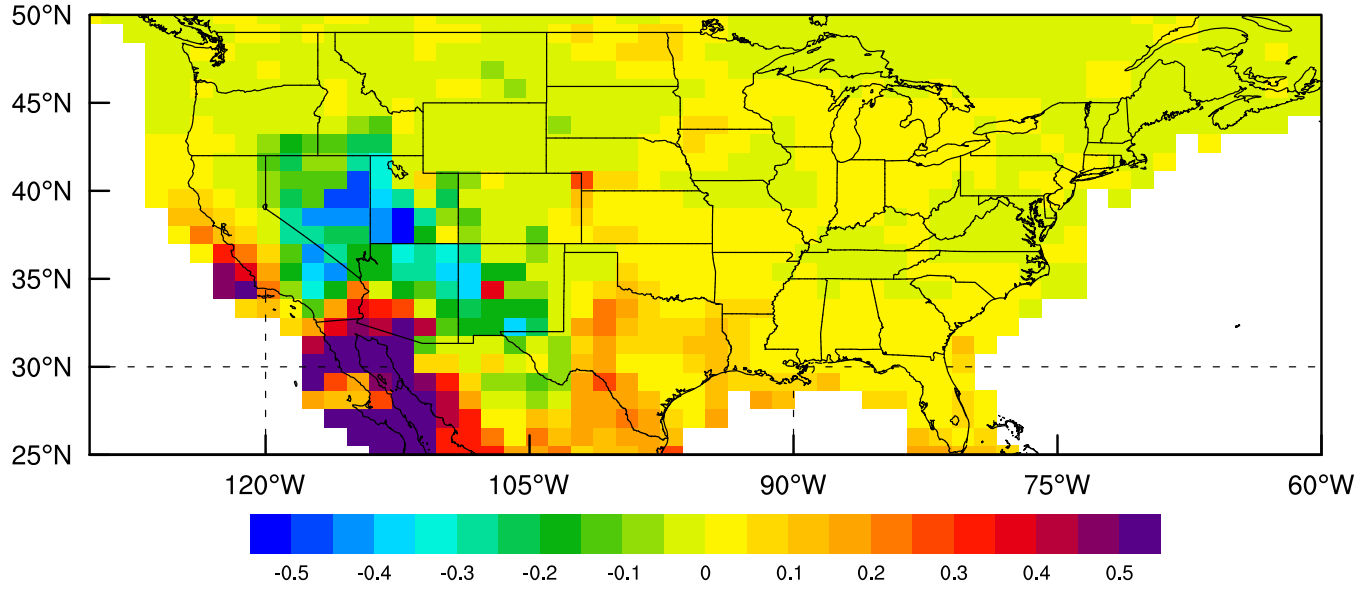
Figure S23. Comparison of July-September mean surface bareness and soil wetness (top 15cm) in the US between LM4.1 and LM4.0 (both at C96 resolution).
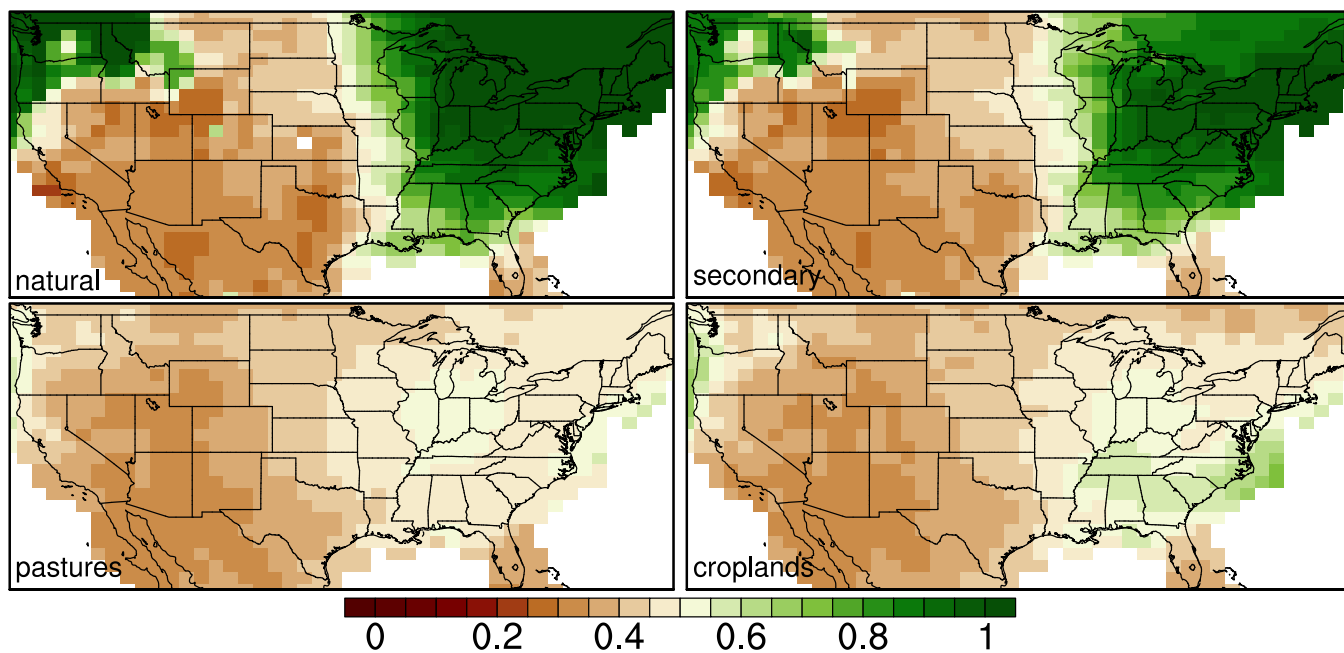
Figure S24. Long-term (1990-2020) summer daytime (9-15 LT) mean ozone dry deposition velocities to natural and secondary vegetation, pastures, and croplands from AM4VR and C96 AMIP simulations.
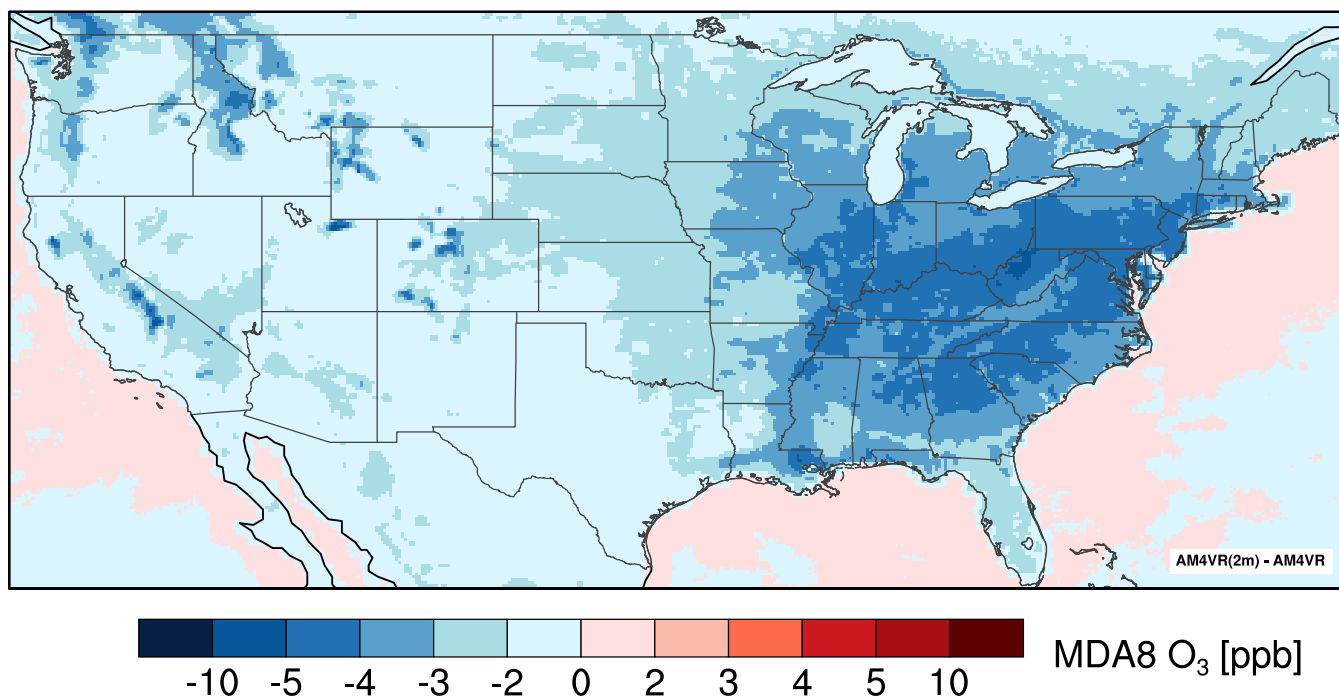
Figure S25. Difference in long-term JJA mean MDA8 ozone concentrations (ppb) in AM4VR sampled at 2 m versus in the 30-m model surface layer.